American Mineralogist, Volume 88, pages 1496–1513, 2003

Experimental hydrothermal alteration of partially metamict zircon

THORSTEN GEISLER,[1,2,4,*] ROBERT T. PIDGEON,[2] REINHARDT KURTZ,[1] WILHELM VAN BRONSWIJK,[3] AND HELMUT SCHLEICHER[1]

[1]Mineralogisch-Petrographisches Institut, Universität Hamburg, Grindelallee 48, 20146 Hamburg, Germany
[2]School of Applied Geology, Curtin University of Technology, PO Box U 1987, Perth 6845, WA, Australia
[3]School of Applied Chemistry, Curtin University of Technology, PO Box U 1987, Perth 6845, WA, Australia
[4]Present address: Institut für Mineralogie, Universität Münster, Corrensstr. 24, D-48149 Münster, Germany

ABSTRACT

We present the results of a series of hydrothermal experiments on grains from two partially metamict zircon samples from Sri Lanka in the temperature range 350 to 650 °C and with different solutions (2 *M* $AlCl_3$, 2 *M* $CaCl_2$, pure H_2O, and a multi-cation solution). Under these conditions, sharply bounded reaction fronts penetrated into the zircon grains and developed complex lobate and rim structures that resemble structures found in natural zircon systems. The reaction zones are characterized by a marked increase in the cathodoluminescence intensity, a decrease of the back-scattered electron emission, and an increased degree of structural order, as revealed by micro-Raman and infrared spectroscopy. Sensitive high-resolution ion microprobe and electron microprobe measurements revealed that the altered areas gained solvent cations (e.g., Ca^{2+}, Ba^{2+}, Mg^{2+}, Al^{3+}) from the solution and lost variable amounts of Zr, Si, Hf, the REE, U, Th as well as radiogenic Pb. A comparison between "dry" and "hydrothermal" annealing trends shows that the kinetics of structural recovery, including recrystallization of the amorphous phase in metamict zircon, is strongly enhanced under hydrothermal conditions. This finding suggests that water "catalyzes" structural recovery processes in metamict zircon. We found that the structure of the reacted areas does not resemble that of crystalline zircon, i.e., is still characterized by a temperature-dependent degree of disorder, which would not be expected if the reaction is controlled by a coupled dissolution and re-precipitation process. Instead, the alteration process can be described best by a diffusion-reaction-recrystallization model. In this model, it is postulated that the diffusion of water into the metamict structure is the driving force for moving recrystallization fronts. We found that the rate and the extent of solid-state recrystallization of the amorphous phase is an important factor in determining the mobility of trace elements. This interpretation is indicated by the observation that trace elements, including U and Th, were preferentially lost during the reaction with a fluid at low temperatures, where recrystallization of the amorphous material was slow or not activated at all. The observed chemical alteration patterns are believed to reflect a competition between the kinetics of long-range diffusion and ion exchange and the kinetics of the short-range diffusion necessary for the recrystallization process.

INTRODUCTION

Since modern imaging techniques such as cathodoluminescence (CL) and back-scattered electron (BSE) imaging have been introduced into zircon geochronology, numerous examples of complex secondary alteration structures such as patchy, isometric, or irregularly curved zones, which overprint apparently older structures, have been observed in natural zircon (e.g., Pidgeon 1992; Pidgeon et al. 1998; Vavra et al. 1996, 1999; Schaltegger et al. 1999; Hoskin and Black 2000; Pidgeon et al. 2000; Tomaschek et al. 2001). These alteration zones are commonly characterized by a lowered Th/U ratio, an enhanced CL emission, transgressive boundaries with primary zircon, and lowered U-Pb ages. They are commonly interpreted to be the results of recrystallization of primary zircon. However, it is still a matter of debate whether recrystallization was triggered by external fluids (e.g., Pidgeon 1992; Pidgeon et al. 1998; Vavra et al. 1999; Pidgeon et al. 2000) or is unrelated to crystal-fluid interaction (Pidgeon et al. 1998; Hoskin and Black 2000). Understanding the origin of these secondary alteration structures as well as the physical-chemical conditions under which they were produced is essential for a reliable geological interpretation of U-Pb ages determined on these structures by microprobe techniques, but also crucial for the evaluation of the suitability of zircon as a potential host material for the immobilization of weapons-grade Pu (e.g., Ewing et al. 1995).

The radioactive decay of U and Th in zircon causes structural damage, which can strongly affect its bulk physical properties (e.g., the density and hardness) (e.g., Murakami et al. 1991). Studies on natural zircon have shown that radiation damage (metamictization) significantly decreases the stability of zircon against aqueous solutions as indicated by an increased loss of radiogenic Pb from metamict zircon (e.g., Silver and Deutsch 1963; Geisler and Schleicher 2000). Two simultaneous processes are responsible for the structural damage: the emission of an α-particle causes the displacement of several hun-

* E-mail: tgeisler@nwz.uni-muenster.de

0003-004X/03/0010–1496$05.00

dred atoms, whereas the recoil of the radiogenic atom produces several thousand atomic displacements within the lattice (e.g., Weber et al. 1994; Farnan and Salje 2001). On the mesoscopic scale, the process of metamictization of a crystalline zircon is characterized by the transformation from an initial stage where isolated amorphous domains are surrounded by slightly disordered crystalline material to a damage level where a few isolated and heavily damaged, nano-crystalline islands or remnants occur in an amorphous matrix (e.g., Murakami et al. 1991; Weber et al. 1994). The crystalline-to-amorphous transformation has recently been described as a geometrical phase transition (Salje et al. 1999). During this transition, the amorphous domains start to form percolating clusters at the first percolation point, whereas at the second percolation transition, the crystalline domains cease to be interconnected. Recent XRD, NMR, and IR studies (Ríos et al. 2000; Farnan and Salje 2001; Zhang and Salje 2001), as well as molecular simulations (Trachenko et al. 2002), indicate that amorphization occurs directly within the recoil cascade. It has been shown experimentally, however, that the structure of both "phases" varies on the atomic scale with increasing degree of self-irradiation. XRD measurements, for example, revealed that the unit-cell volume increases with increasing α-decay dose, which results from an increasing defect density inside the crystalline material (e.g., Murakami et al. 1991). Also, the amorphous phase becomes increasingly polymerized during progressive self-irradiation (Farnan and Salje 2001).

Short-time laboratory heating of a partially metamict zircon to temperatures up to about 700 °C induces only the recovery of the disordered crystalline remnants, i.e., the removal of defects inside the crystalline material, whereas at higher temperatures or longer annealing times, epitaxial recrystallization of the amorphous phase takes place (e.g., Colombo et al. 1999; Capitani et al. 2000; Zhang et al. 2000a, 2000b; Geisler et al. 2001a; Geisler 2002). In heavily metamict crystals, the amorphous phase decomposes to ZrO_2 and SiO_2 before new $ZrSiO_4$ crystallizes (e.g., Capitani et al. 2000; Zhang et al. 2000a, 2000b).

It has been shown previously that the interaction of partially metamict zircon with hydrothermal fluids can be effective in disturbing its U-Th-Pb system (Pidgeon et al. 1966, 1973, 1995; Sinha et al. 1992; Rizvanova et al. 2000; Geisler et al. 2001b, 2002). Geisler et al. (2001b) reported the formation of secondary rim structures similar to those found in natural zircon by treating metamict zircon crystals from Sri Lanka with a 2 *M* $CaCl_2$ solution at 450 °C for one month. These authors suggested that the infiltration of water, resulting in loss of radiogenic Pb and gain of Ca, catalyzed recrystallization, which probably prevented significant dissolution of metamict zircon. More recently, Geisler et al. (2002) observed sharply bounded reaction rims around a partially metamict zircon, which result from the reaction with a 2 *M* $AlCl_3$ and a 1 *M* HCl-$CaCl_2$ solution at 175 °C for less than two months. The recovery process at low fluid temperatures was interpreted to be limited to defect annealing inside the disordered crystalline remnants with little, if any, recrystallization of amorphous domains, as indicated by Raman spectroscopy. The limited recovery had apparently a profound effect on the stability of U and Th, which were extensively removed from the reaction zones, compared with the comparatively high stability of these cations in the 450 °C-experiments of Geisler et al. (2001b). The enhanced susceptibility of metamict zircon to lose Pb, U, and Th at low temperatures in the presence of a fluid, where structural recovery is minimal, was a significant result from that study and can explain loss of Pb, and possible U, from weathered zircon crystals (e.g., Stern et al. 1966).

The purpose of the present paper is to report further results from a series of hydrothermal experiments with partially metamict zircon samples from Sri Lanka at temperatures between 350 and 650 °C using different solutions as reactive fluid. The structural, chemical, and isotopic alteration of the experimental product was characterized by cathodoluminescence (CL) and back-scattered electron (BSE) imaging, Raman and infrared spectroscopy (IR), electron microprobe (EMP) and sensitive high-resolution ion microprobe (SHRIMP) analyses. The data now enable us to propose a model for hydrothermal alteration of metamict zircon, and to demonstrate that zircon-fluid interaction can produce a variety of reaction/recrystallization structures.

Experimental and analytical details

Analytical methods

Quantitative analysis of the starting composition and experimental products were carried out with a Cameca Camebax EMP equipped with three wavelength-dispersive spectrometers. The acceleration voltage was 20 kV at 100 nA beam current. Counting times of a single spot analysis were 10 s for Zr*L*α and Si*K*α, 20 s for Hf*M*α, Y*L*α, Ca*K*α, Ba*K*α, Mg*K*α, Al*K*α, and P*K*α, and 60 s for U*M*β, Th*M*α, Yb*L*α, Er*L*α, K*K*α, and Na*K*α for the peak and the background. The spot size was about 1–2 μm. The 2σ counting errors for UO_2 and ThO_2 were 12% and 25% at 0.15 wt% and 0.10 wt%, respectively. The background calibration approach of Geisler and Schleicher (2000) was used for U and Th analysis. A natural, homogneous zircon from Sri Lanka, containing 2454 ± 87 (2σ) ppm U and 810 ± 21 (2σ) ppm Th, as analyzed by SHRIMP, was used as standard for the U and Th measurements. The errors of the U and Th concentrations in this zircon were estimated from repeated SHRIMP measurements and thus reflect its homogeneity, but not the accuracy, which strongly depends on the homogeneity of the SHRIMP standard (CZ3).

CL and BSE imaging was performed with a Philips XL30 scanning electron microscope equipped with a K.E. Developments Limited CCD-Si cathodoluminescence detector. The acceleration voltage was set to 15 keV, and other experimental parameters were adjusted as to get the maximal CL contrast in the images.

SHRIMP measurements of the starting material and experimental products were made during three analytical sessions at the WA Consortium SHRIMP II at the Curtin University of Technology in Perth, using techniques described in DeLaeter and Kennedy (1994) and Nelson (1997). A primary O_2^- beam was focused to a 25 to 50 μm diameter area on to the target zircon. The mass resolution was about 5000 in all sessions, which was sufficient to resolve isobaric interferences. Measured U/Pb ratios were corrected following Claoué-Long et al. (1995) from ten regular analysis of the standard zircon CZ3 (Pidgeon et al. 1994) over each 24-hour analytical session. The $^{206}Pb/^{238}U$ calibration error was between 2.5 and 3.5%. Measured isotopic ratios were corrected using Broken Hill Pb composition using the ^{204}Pb correction method (Compston et al. 1984).

Laser-Raman spectra were collected with an ISA LabRam dispersive Raman spectrometer using the 632.187 nm line of a He-Ne laser. The scattered Raman light was analyzed with a charged-coupled device (CCD) detector after being dispersed by a grating of 1800 grooves per mm. A 100× objective (N.A. = 0.9) was used on a BX-40 microscope. The spectral resolution was 2.5 cm^{-1}. A confocal hole of 300 μm was used for measurements on the experimental products. The lateral spatial resolution was about 1–2 μm. Raman measurements were made prior to the electron measurements to avoid any effects of electron bombardment on the structure. The frequency and linewidth (given as full-width at half-maximum) of the asymmetrical $v_3(SiO_4)$ stretching band was used for quantitative treatment of the Raman data (see Nasdala et al. 1995). Details about the least-squares fitting procedure and possible errors associated with this procedure,

as well as the method used to correct the fitted linewidth of the $\nu_3(SiO_4)$ band for instrumental broadening, are presented elsewhere (Geisler et al. 2001a, 2003).

Unpolarized reflectance infrared spectra were recorded with a Bruker Equinox 55 spectrometer in the frequency region between 600 and 6000 cm^{-1}. A total of 512 scans were made with a spectral resolution of 4 cm^{-1} on an A590 microscope, by narrowing the beam with a 50 μm aperture.

The starting material

Two alluvial zircon crystals from Sri Lanka (CZ25, HZ5) were used as the starting material for the present study. Whereas crystal CZ25 is translucent brown and HZ5 is dark green, the two zircon samples appeared homogeneous in transmitted light with no evidence of internal zoning or other structures. Both samples have no detectable (by EMP) amounts of Ca, Al, Na, K, Ba, or Mg (Table 1), but have U and Th contents, determined by SHRIMP, of 3110 ± 612 ppm and 720 ± 274 ppm (CZ25), and 2396 ± 59 ppm and 701 ± 27 ppm (HZ5), respectively, which agree well with those determined by EMP analysis on different parts of the samples (Table 1). The high empirical error for the U and Th concentration of sample CZ25 indicates that this sample is not homogeneous. This item will be discussed in more detail in later sections. The $^{207}Pb/^{206}Pb$ ages of sample HZ5 and CZ25 are 542 ± 5 and 524 ± 5 Ma (2σ), respectively. Both zircons are partially metamict, as indicated by broadened and frequency-shifted Raman and IR bands (cf., Nasdala et al. 1995; Zhang et al. 2000b, 2000c; Zhang and Salje 2001). Based on the cumulative α-decay dosage, calculated from the $^{207}Pb/^{206}Pb$ age and the U and Th concentration obtained from SHRIMP U-Pb measurements (HZ5: $4.7 \pm 0.1 \times 10^{18}$, and CZ25: $5.9 \pm 1.1 \times 10^{18}$ α-decays/g), the radiation damage of both samples already crossed the first percolation point proposed by Salje et al. (1999), i.e., amorphous domains form interconnected clusters. Sample CZ25 is only slightly more damaged than sample HZ5 (see Geisler et al. 2001a; Geisler et al. 2002), i.e., it contains ~20% crystalline remnants located in an amorphous matrix compared with ~30% in sample HZ5, as estimated from the α-decay dose and the calibration given by Ríos et al. (2000).

The two starting zircon samples were gently crushed, and fragments used for the experiments were abraded to remove sharp edges. Some grains were polished to produce a single flat surface. After experiments, polished grains were cut perpendicular to the polished surface to measure the reaction rim thickness.

Hydrothermal experiments

Both zircon samples were used for four different series of experiments, which were designed to study the effect of a hydrothermal treatment on metamict zircon and, in particular, the influence of fluid composition, time, and fluid temperature on fluid-zircon interaction (Table 2). The main set of experiments was made with a 2 *M* $CaCl_2$ and 2 *M* $AlCl_3$ solution. To investigate the significance of ionic size and charge on the secondary incorporation of non-formula elements in metamict zircon, we subjected zircon grains to high-temperature (600 °C, experiment no. 4g, Table 2) in a chloride solution containing equal molar concentrations (0.1 mol/L) of six cations, (Na^+, K^+, Mg^{2+}, Ca^{2+}, Ba^{2+}, and Al^{3+}).

The high-temperature series of experiments was carried out in standard cold-seal hydrothermal pressure vessels using gold capsules. A second set of experiments at 350 °C was carried out in sealed silica tubes. Details of the gold capsule experiments are given in Geisler et al. (2001b). The silica tubes were 10 cm long with an internal diameter of 5 mm and a wall thickness of 2.5 mm. The tubes were loaded with 20 abraded zircon grains (~100 to ~500 μm in diameter) and ~0.5 mL solution and sealed with a gas flame, while cooling the other end with liquid nitrogen. The sealed silica tubes were placed upright in bore holes within a block of aluminum, which was put in a low-temperature furnace. The temperature was controlled and monitored by K-type thermocouples, which were placed in special boreholes in the aluminum block reaching the lower ends of the silica tubes. It is important to note that pyrophyllite [$Al_2Si_4O_{10}(OH)_2$] precipitated from the solution, indicating that silica went into the solution, which changed the activity of $Si(OH)_4$ during the experiment. The temperature was constant within ±2 °C over the whole experimental duration. The resulting fluid pressure was estimated to be ~250 bar.

RESULTS

Reaction structures as revealed by BSE and CL imaging

The effects of the hydrothermal experiments on four to five grains from each experiment were studied initially by optical microscopy and then by means of observed changes in the CL and BSE emission. Following the high-temperature experiments in gold tubes (Table 1), grains of sample CZ25 lost their transparency and color and appeared milky white (Fig. 1a). Grains of the less-metamict sample HZ5 also lost their color, but were still transparent (Fig. 1b). CL and BSE images of four to five grains from each experiment reveal that grains of both samples from all experiments, including those with pure H_2O at 600 °C (Fig. 1o), exhibit complex alteration features (Fig. 1b-1q). We would like to emphasize that the examples shown in Figure 1 represent an essentially representative selection from the variety of observed reaction textures. The reaction domains are characterized by increased CL and lowered BSE intensity with respect to the apparently unreacted cores and the starting material (compare Figs. 1c and 1d, as well as Figs. 1j and 1k). The boundary between the reaction zones and cores, as identified by these imaging techniques, is sharp in all experiments. The boundary morphology and internal structure of reaction zones are more diverse and complex than those observed in previous experiments (Geisler et al. 2001b, 2002). The alteration zones can occur as thin relatively homogenous (uniform CL) reaction zones or rims, as well as lobate and lacework-like reaction areas, extending inward from the fluid-mineral interface (e.g., Figs. 1b and 1c). However, in the high-temperature experiments (>550 °C) many grains of sample CZ25, although as large as 300–500 μm in diameter, have almost completely reacted with the fluid (Figs. 1e–1g). Only small relicts of apparently unreacted zircon can be detected by their still low CL intensity within the interior of these grains. These unreacted remnants are surrounded by a diffuse halo with a slightly darker CL intensity relative to that of the reacted matrix (Fig. 1e). It is also striking that the CL images of these grains show a banded structure, which is possibly controlled by previously undetected parallel growth zoning in the starting zircon. Particularly intriguing is the example in Figure 1f, which shows a banded structure, truncated at right angles by a younger homogeneous, bright CL domain with a small, non-luminescent remnant of unreacted zircon. Some of the almost completely reacted grains also show a localized, fine and diffuse ring structure, which is unrelated to the parallel-type banding (arrows in Figs. 1f and 1g). A careful inspection of these grains reveals that these structures are located in areas that are located at the limit reached by reaction fronts advancing from all directions. Other grains of sample CZ25 show a simple core-rim (Figs. 1c, 1d) or an alteration pattern of parallel (Figs. 1h) or network-like reaction zones (Figs. 1i). The latter pattern is very similar to those observed in grains of CZ25 treated with a 1 *M* HCl-$CaCl_2$ solution at 175 °C (Geisler et al. 2002). Examples of intrusive lobate-shaped reaction structures are shown to have developed in grains of CZ25 after 1770 hours in 2 *M* $AlCl_3$ at 350 °C (Figs. 1j–1l). In detail, the boundary with unreacted zircon is seen to be highly irregular and interpenetrating (Fig. 1l). A striking feature of the reaction domains in this and similar grains is that they commonly consist of an inner and an outer zone, each with a distinctly different, but uniform CL emission. The outer zone has a relatively low CL intensity compared with a bright CL inner zone (Fig. 1l). This complex reaction structure is not observed in grains of sample HZ5 subjected to the same conditions. A magnified section (Fig. 1m) shows in close detail the

TABLE 1. Average starting composition obtained by electron microprobe and representative analyses from all analyzed experimental products (in wt%)

Sample	CZ25		CZ25			CZ25		CZ25		
Experiment			no. 7			no. 1g		no. 2g		
Temp.			350 °C			554 °C		650 °C		
Solution	Starting material		2M $AlCl_3$			2M $CaCl_2$		2M $CaCl_2$		
Location*	(n = 18)		12	26	48	–	–	a	b	c
Description†			*dr*	*br*	*c*	*r*	*c*	*r*	*r*	*c*
ZrO_2	66.52	±0.32	57.81	64.07	66.90	63.41	65.84	64.68	62.43	66.04
SiO_2	30.47	±0.09	33.38	30.01	30.73	31.28	30.66	30.20	29.91	31.09
HfO_2	1.14	±0.02	0.83	1.09	1.16	1.17	1.11	1.12	1.08	1.12
Y_2O_3	0.22	±0.02	0.05	0.19	0.20	0.16	0.18	0.23	0.19	0.23
P_2O_5	0.12	±0.01	0.10	0.08	0.08	0.12	0.16	0.10	0.07	0.09
Er_2O_3	0.05	±0.02	0.02	0.09	0.05	0.05	0.06	0.08	0.07	0.06
Yb_2O_3	0.10	±0.01	<0.01	0.08	0.11	0.12	0.09	0.08	0.06	0.11
UO_2	0.373	±0.013	0.131	0.419	0.387	0.322	0.356	0.378	0.420	0.341
ThO_2	0.084	±0.020	0.018	0.053	0.072	0.073	0.064	0.082	0.111	0.079
CaO	<0.006		<0.006	<0.006	<0.006	1.155	0.011	0.90	1.24	<0.006
Al_2O_3	<0.005		3.22	0.053	<0.005	<0.005	<0.005	<0.005	<0.005	<0.005
Na_2O	<0.006		–	–	–	–	–	–	–	–
K_2O	<0.007		–	–	–	–	–	–	–	–
BaO	<0.006		–	–	–	–	–	–	–	–
MgO	<0.005		–	–	–	–	–	–	–	–
Total	99.09	±0.34	95.56	96.13	99.68	97.86	98.52	97.84	95.58	99.17
H_20‡	0.91	±0.34	4.44	3.87	0.32	2.14	1.48	2.16	4.42	0.83

Sample	CZ25		HZ5		HZ5		HZ5		HZ5	
Experiment	no. 4g				no. 7		no. 2g		no. 4g	
Temp.	600 °C				350 °C		650 °C		600 °C	
Solution	Multi-cation		Starting material		2M $AlCl_3$		2M $CaCl_2$		Multi-cation	
Location*	20	48	(n = 10)		20	–	6	34	3	40
Description†	*r*	*c*			*r*	*c*	*r*	*c*	*r*	*c*
ZrO_2	65.67	65.77	66.57	±0.17	63.06	66.41	60.99	64.02	60.23	65.89
SiO_2	29.89	31.06	30.86	±0.03	30.27	30.49	29.88	31.08	30.20	31.32
HfO_2	1.18	1.17	1.40	±0.02	1.48	1.49	1.49	1.54	1.54	1.52
Y_2O_3	0.20	0.20	0.10	±0.01	0.06	0.13	0.08	0.14	0.08	0.10
P_2O_5	0.08	0.09	0.04	±0.01	0.06	0.06	0.24	0.04	0.66	0.05
Er_2O_3	0.06	0.06	0.02	±0.02	0.03	0.03	0.04	0.04	0.05	0.04
Yb_2O_3	0.06	0.10	0.04	±0.01	0.05	0.04	0.01	0.04	0.02	0.01
UO_2	0.421	0.400	0.290	±0.005	0.226	0.292	0.303	0.326	0.167	0.271
ThO_2	0.061	0.096	0.081	±0.002	0.052	0.106	0.081	0.076	0.036	0.090
CaO	0.089	<0.006	<0.006		<0.006	< 0.006	0.243	<0.006	0.071	<0.006
Al_2O_3	<0.005	<0.005	<0.005		2.99	< 0.005	0.046	<0.005	0.562	<0.005
Na_2O	0.006	<0.006	<0.006		–	–	–	–	<0.006	<0.006
K_2O	0.032	<0.007	<0.007		–	–	–	–	0.007	<0.007
BaO	0.137	<0.006	<0.006		–	–	–	–	0.020	<0.006
MgO	0.268	<0.005	<0.005		–	–	–	–	0.030	<0.005
Total	98.16	98.93	99.41	±0.18	98.28	99.04	93.39	97.30	93.67	99.29
H_20‡	1.84	1.07	0.59	±0.18	1.72	0.96	6.61	2.70	6.33	0.71

Notes: The errors given for the analyses of the starting material represent the 2σ standard deviation of the mean obtained from n measurements.
(–) = not measured.
* Numbers refer to distance from the surface of the grains in μm. Letters refer to spots marked in Figure 1f.
† *dr* = gray-CL zone, *br* = brigh-CL zone, *r* = reaction zone, *c* = low-CL core.
‡ Calculated by difference.

interaction of external fluids with this zircon as a series of sharply defined, lobate-like reaction fronts with relatively homogeneous CL emission. Another distinctive reaction type was found in all high-temperature experiments with sample HZ5, including the experiment with pure water (Figs. 1n–1q). In these experiments, bright-CL rims with an irregular, ramified, or scalloped boundary with the unreacted core were developed. These reaction rims also exhibit regular patterns of short dark-CL stripes (Figs. 1n, 1o). A BSE image of a magnified section of this structure reveals that the dark-CL stripes correspond to the location of channels or cracks, which are generally oriented at right angles to the reaction front and are found only within the reacted area (Fig. 1p). The low CL emission around these structures may be explained by CL quenching due to surface damage (e.g., Townsend et al. 1999).

Thickness of the reaction zones

Geisler et al. (2001b) found a strong dependence between thickness of reaction rims formed during hydrothermal treatment with a 2 *M* $CaCl_2$ solution at 450 °C for one month and the degree of radiation damage. However, the rim thickness also depends on other factors, including the fluid temperature. The temperature dependence of the thickness of the reaction rims around grains from sample HZ5, as measured on cross-sections through the center of the grains or perpendicular to a polished face, is given for a set of experiments at various temperatures, but otherwise identical conditions (72 h/ 2 *M* $CaCl_2$ sol./1 kbar): 5–10 μm at 554 °C, 11–18 μm at 600 °C, 11–14 μm at 617 °C, and 19–27 μm at 650 °C fluid temperature. Due to the irregularity of the reaction rims of sample CZ25 caused by fracturing and its heterogeneity, it was not possible to ex-

TABLE 2. Summary of experimental conditions

Experiment no.	Fluid	Sample	T (°C)	±(°C)*	P (kbar)	t (h)	Reference
			Teflon bomb experiments				
1t	2 M $AlCl_3$	CZ25	175	±2	<~0.05	1340	Geisler et al. (2002)
2t	1 M HCl+$CaCl_2$						
			Silica tube experiments				
3	2 M $AlCl_3$	HZ5 CZ25	350	±2	~0.25†	504	this study
5	2 M $AlCl_3$	HZ5 CZ25	350	±2	~0.25†	1124	this study
7	2 M $AlCl_3$	HZ5 CZ25	350	±2	~0.25†	1770	this study
9	2 M $AlCl_3$	HZ5 CZ25	350	±2	~0.25†	2300	this study
			Gold capsule experiments				
P9	2 M $CaCl_2$	Z9	450	±2	1.3	744	Geisler et al. (2001b)
P10		Z10					
P11		Z11					
P16		Z16					
1g	2 M $CaCl_2$	CZ25 HZ5	554	±4	1.0	72	this study
7g	2 M $CaCl_2$	CZ25 HZ5	600	±2	1.0	72	this study
3g	2 M $CaCl_2$	CZ25 HZ5	617	±2	1.0	72	this study
2g	2 M $CaCl_2$	CZ25 HZ5	650	±5	1.0	72	this study
4g	Multi-cation solution‡	CZ25 HZ5	585	±2	1.0	72	this study
8g	H_2O	CZ25 HZ5	600	±2	1.0	170	this study

* Maximal temperature fluctuations as registered during the experiments.
† Estimated from the specific volume of water at 350 °C.
‡ Composition: 0.1mol/l Na^+, K^+,Ca^{2+}, Mg^{2+}, Ba^{2+}, Al^{3+}, and 1.1 mol/l Cl^-.

tract meaningful and unambiguous quantitative information about their thickness. However, we emphasize that the reaction areas can extend more than 250 μm into the grains (Fig. 1). Although the actual difference in the degree of radiation damage between both samples as quantified by the α-decay dose is hardly significant, it is evident that in all experiments and in all investigated zircons, the amount of reacted zircon is significant higher in grains from sample CZ25 than from sample HZ5. This result suggests that the difference in the accumulated radiation damage of both samples is high enough to result in a significant different stability against hydrothermal solutions.

Chemical alteration

General observations. EMP point measurements and line scans reveal that complex chemical exchange reactions occurred in the reacted zones of hydrothermally treated grains of both samples when compared with unreacted zircon (no detectable CL change) and the starting material (Table 1; Figs. 2 and 3). An important feature of the EMP analyses of the reaction zones is that they all have significantly lower analytical totals compared with those of the starting material and the low-CL cores (Table 1). In the high-temperature experiments (>350 °C) with a 2 M $CaCl_2$ solution, grains of both samples experienced significant losses of Zr and, in all cases, a gain of Ca from the solution, whereas only minor or no detectable loss of Si, Hf, Y, Yb, Er, U, and Th was observed. Three analyses located on different parts of the highly reacted and banded CZ25 grain f (Fig. 1f; experiment no. 2g) show that, in contrast to the banded (i.e., reacted) areas (analyses *a* and *b* in Table 2), the low-CL remnant (analysis *c* in Table 2) has retained its original composition. The significantly higher U and Th concentrations in analysis *b* compared to that labeled *a* probably reflect original differences within the untreated grain.

The set of experiments with $AlCl_3$ solution at 350 °C produced significantly different chemical changes when compared with the high-temperature experiments. As already mentioned, hydrothermal treatment of grains from sample CZ25 in a 2 M $AlCl_3$ solution at 350 °C produced a gray- and bright-CL reaction rim, which are also characterized by a distinct chemical alteration pattern. The gray-CL outer zone of the reaction rims experienced extensive loss of Zr, U, Th, Y, Yb, and Er, a significant gain of Al (up to 17,000 ppm Al), and a relative enrichment of Si. In contrast, the bright-CL inner zone suffered only a slight loss of Zr, Si, Y, Yb, Er, and Th (Fig. 2b). The same hydrothermal treatment produced reaction rims around sample HZ5, which lost Zr, Y, Th (Table 1), and minor amounts of Si (Fig. 4b).

An important observation is that the EMP line scan through a reaction rim of a grain from sample HZ5 treated for 72 hours in a 2 M $CaCl_2$ solution at 650 °C show a non-uniform distribution of solvent and solute cations with the reaction rim (Fig. 2a). In particular the Zr, Si, and Ca concentrations define diffusion-like profiles. Also the concentration profiles through the two-stage rim around grains of sample CZ25 subjected to $AlCl_3$ solution at 350 °C do not define a sharp boundary to the apparently unreacted core (Fig. 2b). However, at higher fluid temperatures, the concentration profiles usually define a sharper boundary with the low-CL core, although the chemical gradients are usually not fully congruent with the rim-core bound-

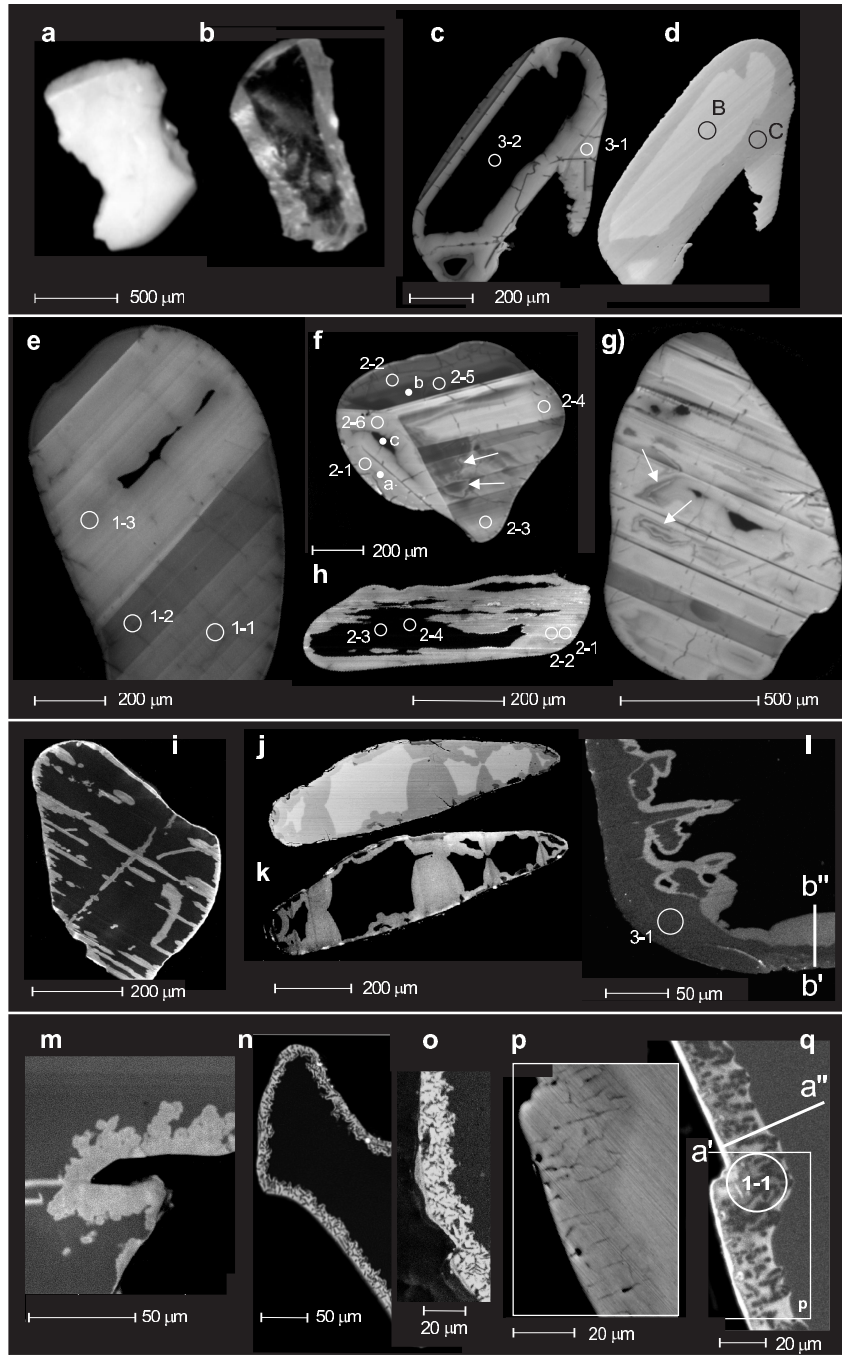

FIGURE 1. Experimentally produced recrystallization structures of hydrothermally treated grains of sample HZ5 and CZ25 as imaged by optical microscopy (OM), cathodoluminescence (CL), and back-scattered electron (BSE) imaging techniques. (**a**) and (**b**) OM images of whole grains of sample CZ25 and HZ5, respectively (experiment no. 7g). Note that the grain of sample CZ25 is milky white, whereas that of sample HZ5 does not show any optically visible signs of alteration. (**c**) CL and (**d**) BSE image of the same grain of sample CZ25 (experiment no. 2g). (**e**) to (**g**) CL images of grains of sample CZ25 (experiment no. 2g). The arrows in Figures 1f and g point to diffuse ring structures. (**h**) and (**i**) CL images of grains of sample CZ25 (experiment no. 1g). (**j**) BSE and (**k**) CL image of the same grain of sample CZ25 (experiment no. 7), (**l**) CL image of a grain of sample CZ25 (experiment no. 7). The electron microprobe traverse shown in Figure 3b is marked in the CL image. (**m**) CL image of a grain of sample HZ5 (experiment no. 3). (**n**) CL image of a grain of sample HZ5 (experiment no. 2g). (**o**) CL image of a grain of sample HZ5 treated in pure water at 600 °C (experiment no. 8g). (**p**) BSE image of a grain of sample HZ5 (experiment no. 2g). The image shows a part of Figure 1q. (**q**) CL image of the same grain shown in Figure 1p. The electron microprobe traverse shown in Figure 3a is marked in the CL image. The location of SHRIMP and electron microprobe spots are marked by white open and filled circles, respectively. Large open circles in Figure 1c labeled B and C mark spot locations of reflectance IR measurements shown in Figure 7a.

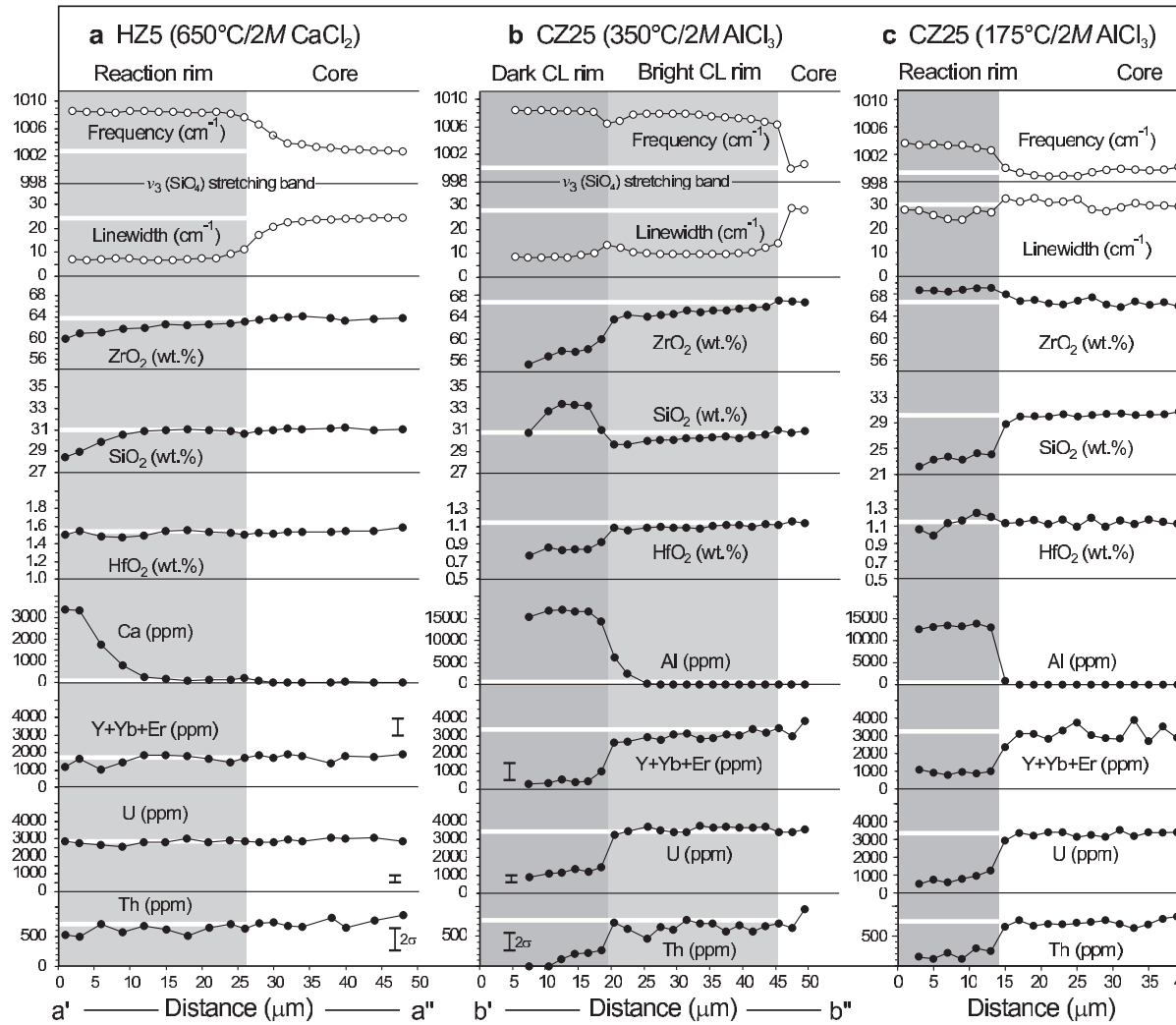

FIGURE 2. Raman frequency and linewidth profiles of the $\nu_3(SiO_4)$ stretching mode (open circles) and electron microprobe concentration profiles (filled circles) across hydrothermal reaction zones. (**a**) Grain of sample HZ5 (experiment no. 2g), (**b**) of sample CZ25 (experiment no. 7), and (**c**) of sample CZ25 (experiment no. 1t) (data from Geisler et al. 2002). White bar inside the reaction rims mark the average of the core measurements as a visual guide. The measured traverses in Figure 3a and b are shown in the CL images of Figure 1q and 1l, respectively.

ary marked by the CL contrast (Fig. 3a). The complex behavior of elements in these reaction zones shown in the EMP line scans will be analyzed further in the following discussion.

The behavior of non-formula elements. The multi-cation experiment results (experiment no. 4g, Table 2) provide some insights into controls on the admission of trace elements into the radiation-damaged zircon structure. The EMP analyses (Table 1) reveal that the concentrations of non-formula cations in the reaction zones of sample CZ25 (ignoring the different behavior of Al for the time being) is higher than in the reaction rims of sample HZ5 (Fig. 3b). This observation indicates that degree of radiation damage has an impact on the secondary incorporation of non-formula elements during zircon-fluid interaction. It is further evident from Figure 3b that, under the given experimental conditions, the secondary incorporation of non-formula cations depends largely on ionic radius and to a lesser extent on ionic charge. The unsystematic behavior of Al in sample CZ25, however, is currently not understood. We note here that the observed ionic-size (and charge) dependence is in agreement with the observation that the Na concentration in hydrothermally altered, natural zircon is usually several orders of magnitude lower than the Ca content (commonly below the detection limit of the EMP and thus rarely included in analytical investigations) (e.g., Medenbach 1976; Geisler and Schleicher 2000), although Na^+ is—along with Ca^{2+}—the most important cation in natural brines.

The relationship between SiO_2 and ZrO_2. The relationships between SiO_2 and ZrO_2 for reaction zones generated under the different experimental conditions, including the results of the low-temperature experiments of Geisler et al. (2002), are shown in Figure 4. It can be seen in this figure that three different reaction trends can be distinguished for sample CZ25. The first trend is marked by a slight apparent loss of Zr and Si in nearly stoichiometric proportions when compared with data

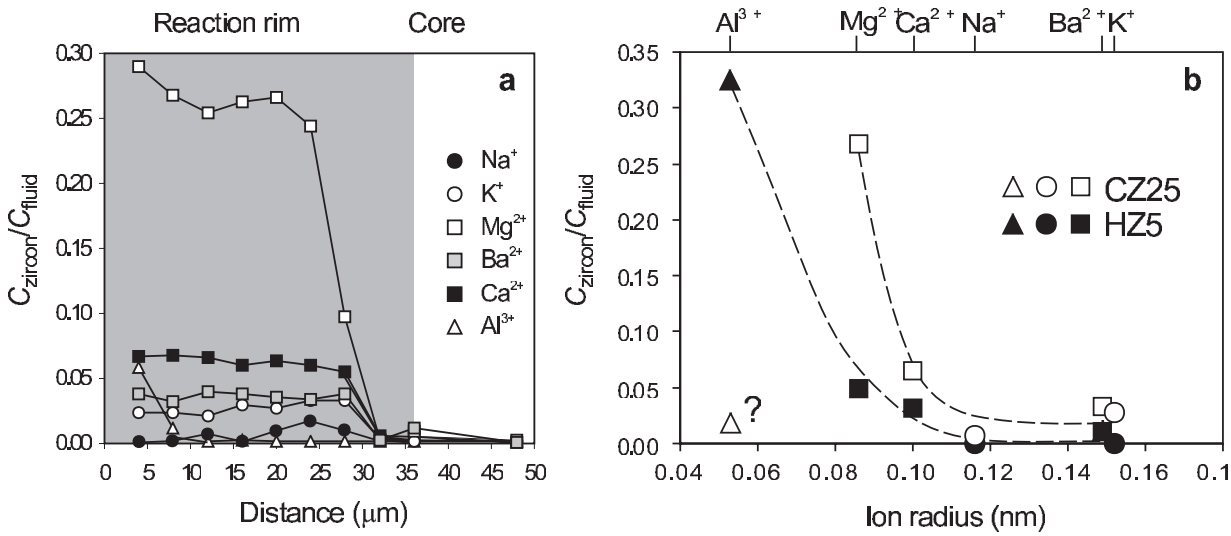

FIGURE 3. (**a**) Zircon-fluid partition coefficients, C_{zircon}/C_{fluid}, of five different cations plotted as a function of the distance from the surface for a hydrothermally treated grain of sample CZ25. (**b**) Average C_{zircon}/C_{fluid} for the same cations as in Figure 4a plotted as a function of the ionic radius for reaction zones from grains of sample CZ25 and HZ5. Stippled curves are guides to the eye only. All zircon grains were treated in a multi-cation solution for 72 hours at 585 °C and 1 kbar fluid pressure (experiment no. 4g). Ionic radii are from Shannon (1976).

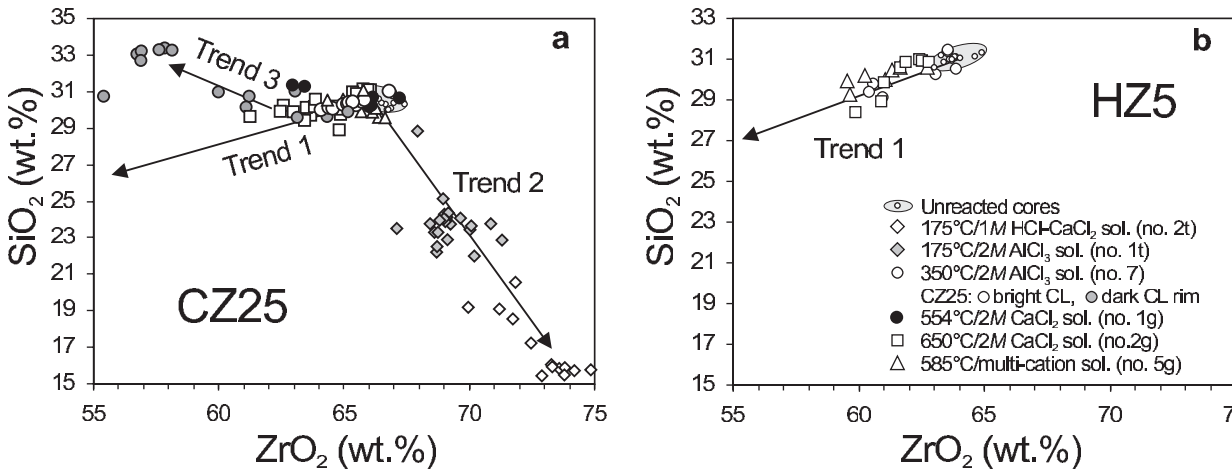

FIGURE 4. Plot of SiO_2 vs. ZrO_2 showing electron microprobe analyses of the starting material and reaction zones formed under different hydrothermal conditions. (**a**) Grains of sample CZ25. (**b**) Grains of sample HZ5. Data from the 175 °C experiment with sample CZ25 are from Geisler et al. (2002).

from the starting material and the core areas. The second trend for this sample is described by the low-temperature data from experiments in a 2 *M* $AlCl_3$ and a 1 *M* HCl-$CaCl_2$, solution and is characterized by a relative enrichment of Zr and an extreme loss of Si (Geisler et al. 2002). The third trend is directed to lower ZrO_2 and higher SiO_2 compared with the starting material, and is defined by data from reaction zones of grains treated in 2*M* $AlCl_3$ solution at 350 °C in silica tubes. Here the data from the bright-CL rim, however, follow the first reaction trend, whereas those with the less-enhanced CL intensity define the third trend that runs toward higher SiO_2 and lower ZrO_2. Note that all the data points from hydrothermally treated grains of sample HZ5 fall on a single trend (Fig. 4b). We note here that the SiO_2 vs. ZrO_2 relationship in many natural altered zircons follow trend 1 in Figure 4 (e.g., Medenbach 1976; Mathieu et al. 2001; Geisler et al. 2003). The significance of these trends will be considered further in later sections.

Disturbance of the U-Th-Pb isotopic system. SHRIMP U-Pb isotope data from a number of unreacted cores and reaction zones from different experiments are presented in Table 3[1] and on conventional concordia diagrams (Fig. 5). Whereas core areas are concordant within analytical uncertainty, all analyzed

[1]For a copy of Table 3, document item AM-03-039, contact the Business Office of the Mineralogical Society of America (see inside front cover of recent issue) for price information. Deposit items may also be available on the American Mineralogist web site at http://www.minsocam.org.

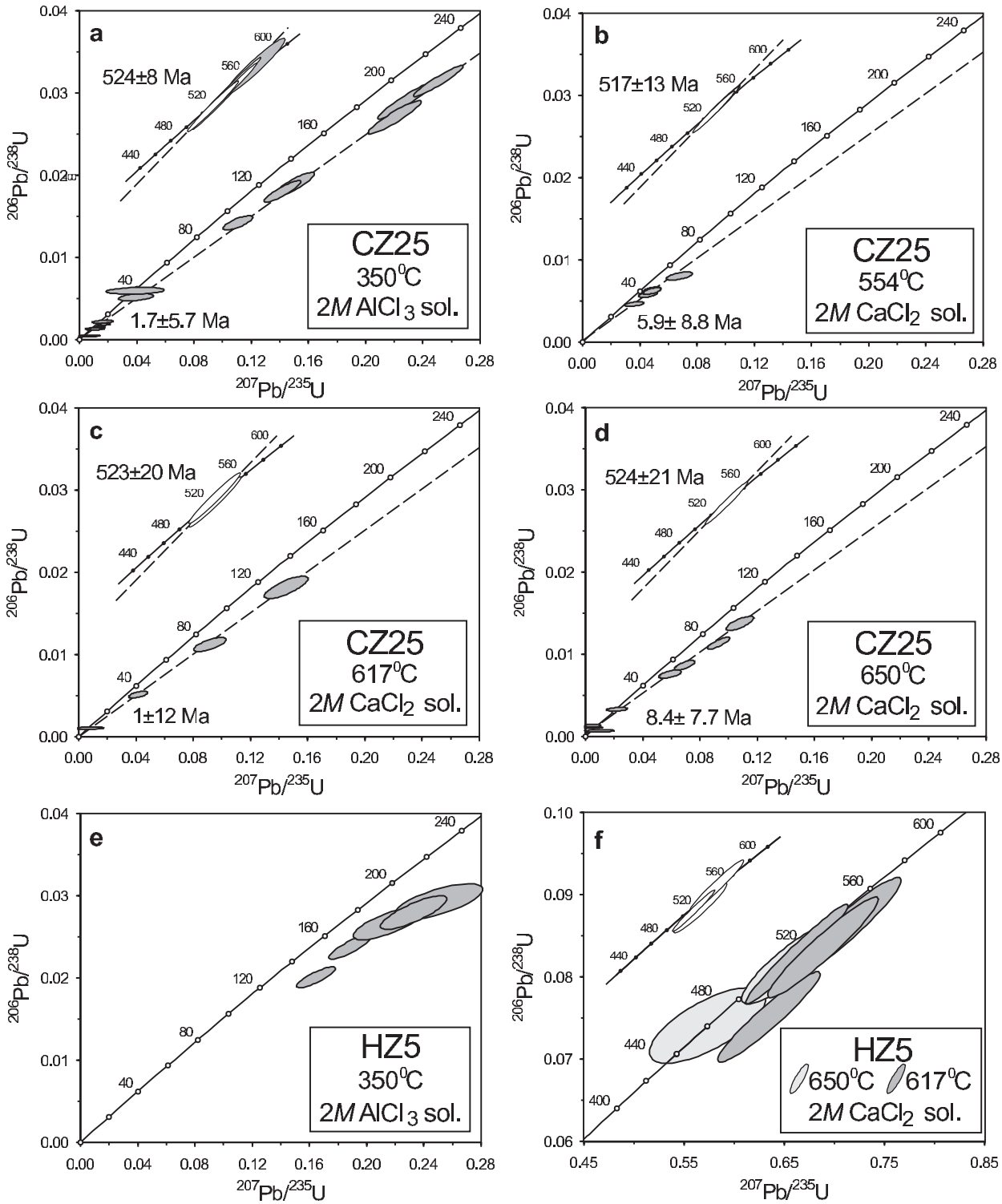

FIGURE 5. Concordia diagrams showing SHRIMP data from the starting material (open ellipses) and reaction zones (shaded ellipses) formed under different hydrothermal conditions. (**a**) to (**d**) Data from grains of sample CZ25 and (**e**), (**f**) of sample HZ5.

reaction zones of sample CZ25 have undergone a significant disturbance of their U-Pb system (Figs. 5a, 5d). Some points are almost completely reset and the isotope data define linear discordance patterns, which project to the origin of the concordia diagram. This discordance is due to a severe loss of radiogenic Pb during the experiments, which exceeded 90% in eight analyses on grains from the 350 °C experiments and reached ~80% in the high-temperature experiments (Table 3). However, a single analysis from a gray-CL rim of a 350 °C-experiment (no. 3-Z25-4-1) is concordant, although large amounts of U, Th, and Pb have been lost (Fig. 5a, Table 3). Note that the U-Pb ages are increased significantly (e.g., $^{206}Pb/^{238}U$ age: 568 ± 17 Ma). The gray-CL rims also experienced a significant change in the Th/U ratio (Fig. 6, Table 3). The loss of Pb, i.e., the discordance pattern, of the 350 °C experiments shown in Figure 5a appears to be independent of the duration of the experiment (Table 3). In response to the high-temperature experiments, some reaction zones of the grains of CZ25 also lost minor amounts of U and Th (Table 3, Fig. 6). However, due to the heterogeneity of the sample, it is difficult to decide whether the U and Th loss is real. There appears to be a slight tendency for a higher Th loss at a given fluid temperature (see Fig. 6). A further important observation is that the loss of U and Th from the reacted areas of sample CZ25 tend to be the highest in the low-temperature experiments (Fig. 6).

Reaction areas of grains treated with a 2 *M* $AlCl_3$ solution at 350 °C for 72 hours experienced losses up to 80% Pb, up to 45% U, and up to 53% Th (Figs. 5e; Fig. 6; Table 3), which are similar to the behavior of the bright-CL zones of sample CZ25 formed under the same conditions. Keeping in mind that we have collected only a limited amount of analytical data from sample HZ5, there also appears to be a tendency for higher U and Th loss at lower fluid-temperatures as observed for sample CZ25 (Fig. 6). However, in experiments conducted at higher fluid temperatures, the behavior of the U-Th-Pb system of sample HZ5 is slightly different from that seen in sample CZ25 (Figs. 5 and 6). The main difference is that we could also detect significant loss of U, Th, and Pb from the reacted areas formed at fluid temperatures as high as 617 °C (Fig. 6). Surprisingly, the reaction rims formed in the 650 °C-experiment, on the other hand, did not lose significant amounts of U, Th, and Pb, so that they still give concordant U-Pb isotope ratios (Fig. 5f). Furthermore, the U-Pb isotope data from reaction areas formed at 617 °C are concordant or plot close to the concordia. However, strictly speaking, this is a "pseudo" U-Pb concordance (Fig. 5f), as minor loss of U and radiogenic Pb occurred simultaneously (Table 3).

Structural alteration

The reaction rims and zones. Reflectance IR and micro-Raman measurements were carried out on the reaction zones, cores, and untreated samples to investigate the process of structural recovery of the metamict zircon under hydrothermal conditions and its role in the overall chemical exchange process. Figure 7 shows Raman and reflectance infrared spectra from reaction zones developed on grains of sample CZ25

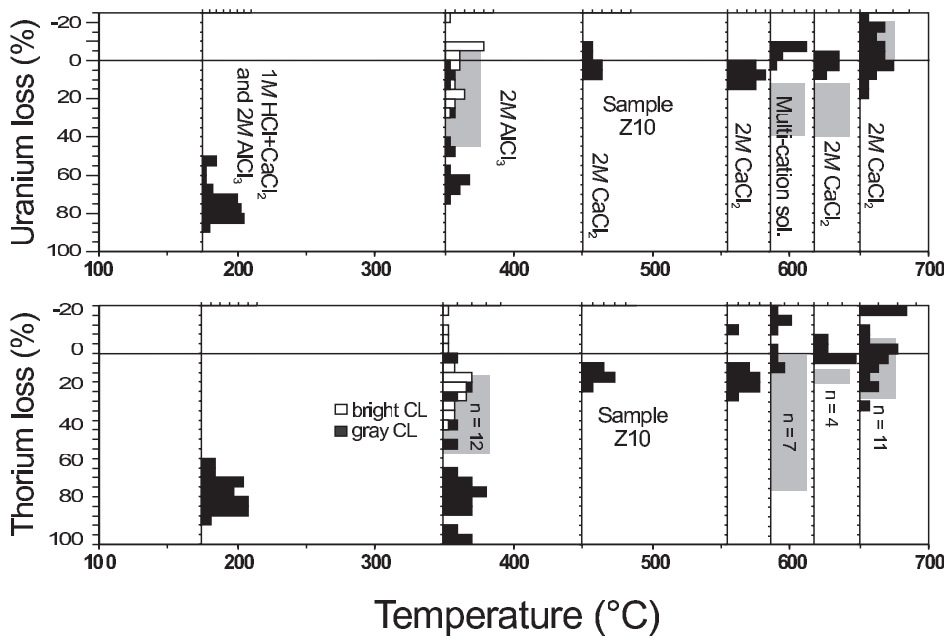

FIGURE 6. The loss of U and Th from reaction zones determined by SHRIMP and electron microprobe analyses as a function of the fluid temperature for sample CZ25 (histograms) and HZ5 (gray fields enclose the minimum and maximum value). Also shown for comparison are data for the 450 °C experiment with a similar metamict zircon from Sri Lanka (sample Z10; Geisler et al. 2001b), and U and Th data from 175 °C-experiments of Geisler et al. (2002). To reduce the influence of the heterogeneity of sample CZ25, the U and Th loss of each reaction zone of was estimated by using the average U and Th concentration of the core determined for each grain. The fields of sample HZ5, however, were constructed by using the average U and Th concentration of the untreated sample, as obtained from SHRIMP and EMP measurements.

under hydrothermal conditions compared with a typical spectrum of the starting material and a crystalline reference zircon. The profound impact of the fluid-zircon reaction in causing significant structural recovery is indicated by peak sharpening and a frequency blue shift of the internal (SiO_4) bending and stretching modes (e.g., Zhang et al. 2000a, 2000b). This change can also be seen in the Raman line scans made along the EMP line profiles, showing the frequency and linewidth of the asymmetrical $\nu_3(SiO_4)$ stretching band (Fig. 2). This observation is in general agreement with findings of other hydrothermal experiments using powder XRD analysis (Pidgeon et al. 1995; Rizvanova et al. 2000; Geisler et al. 2001b) or micro-Raman and powder IR spectroscopy (Geisler et al. 2001b, 2002). It is important to note that we did not observe new bands in any of the spectra, indicating that the zircon grains did not significantly decompose to zirconia and silica. This finding contrasts with results from hydrothermal experiments with metamict zircon in an alkaline sodium carbonate solution, where baddeyleiite and a Na-Zr-silicate were detected as reaction products (Rizvanova et al. 2000).

In Figure 8 we have combined all of our new Raman measurements on reaction zones of both zircon samples together with data from Geisler et al. (2002) in a diagram showing the frequency of the $\nu_3(SiO_4)$ stretching band near 1008 cm^{-1} as a function of its width. The Raman measurements from the reaction zones of both samples plot on or close to the "dry" annealing trend determined for sample HZ5 (Fig. 8b; Geisler 2002). This result suggests that the disorder-to-order transformation in a hydrothermal environment is similar to those under dry conditions. However, the recovery processes are activated at significant lower temperatures in a hydrothermal environment (see Fig. 8b). Whereas the first "dry" annealing stage has been interpreted to involve anisotropic defect annealing inside the crystalline domains, the second and third stages are characterized by the epitaxial recrystallization of the amorphous material, resulting in the recovery of the long-range order (e.g., Colombo et al. 1999; Zhang et al. 2000a, 2000b; Geisler et al. 2001a). XRD measurements indicate that the third annealing stage also involves further anisotropic annealing of stable defects responsible for a residual expansion of the *c*-axis inside the crystalline remnants (Geisler 2002). All reaction zones of our new hydrothermal experiments reached the third "dry" annealing stage (Fig. 8). It is important to highlight, however, that structural recovery is not complete. A comparison with Raman measurements on a synthetic reference zircon shows that the structure of the reaction areas does not resemble that of a pristine zircon (see star in Fig. 8).

A significantly different linewidth of the $\nu_3(SiO_4)$ stretching band of reaction zones from both samples, which were formed at 350, 554, and 617 °C (Fig. 8), indicates that the temperature dependence of the structural recovery processes is not the same for both samples. Furthermore, although the degree of structural recovery increases, the data from the $AlCl_3$ and the $CaCl_2$ experiments with sample CZ25 diverge slightly from each other, i.e., the data from the $AlCl_3$ experiments plot at higher frequencies at a given linewidth (Fig. 8a). Because a systematic frequency calibration error can been excluded (some of the Raman data from the annealing experiments under dry conditions were collected during the same session as the data presented here), the observed differences should have a physical significance, which will be discussed further in a later section.

The low-CL cores. An important observation to understanding the inward propagation of the recrystallization fronts is that in the high-temperature experiments, the recovery of the

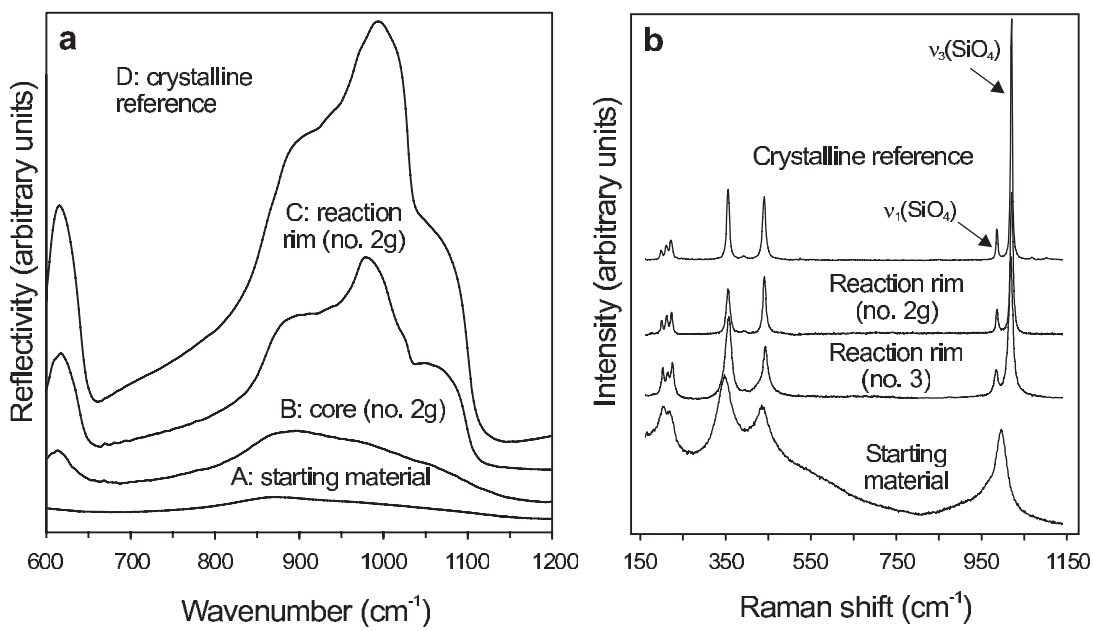

FIGURE 7. (**a**) Typical unpolarized reflectance infrared (spot locations B and C are shown in Figure 1d), and (**b**) Raman spectra of the starting material of sample CZ25, a crystalline reference zircon, and of a low-CL core and reaction zones of sample CZ25 formed under different hydrothermal conditions.The spectra were stacked for clarity.

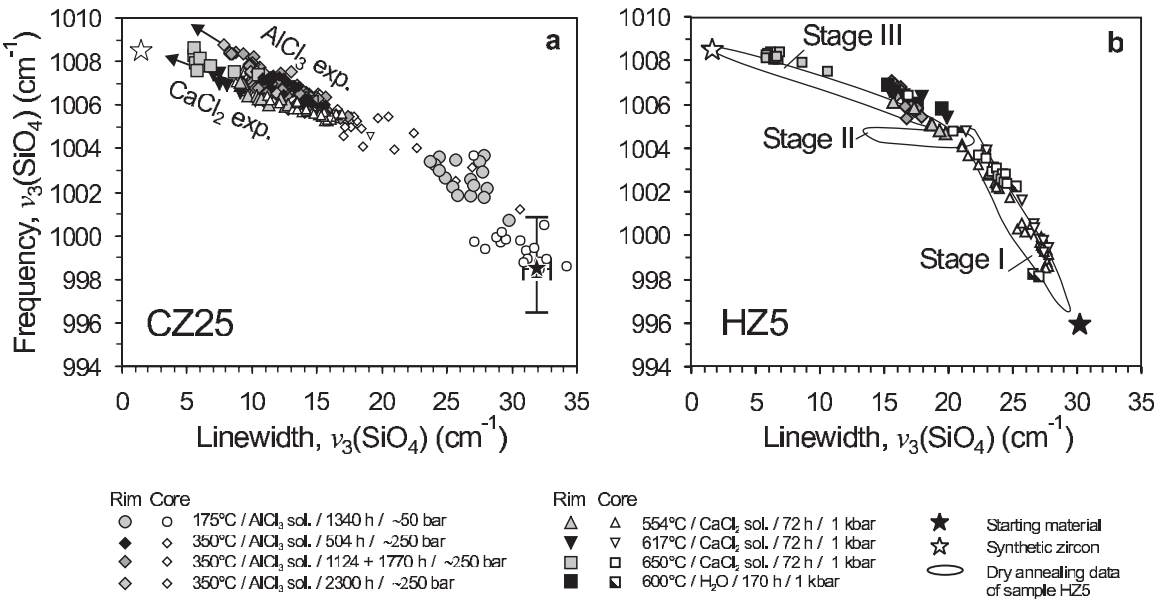

FIGURE 8. The frequency of the asymmetrical $\nu_3(SiO_4)$ stretching band as a function of its width for reaction zones (gray shaded or black symbols) and low-CL cores (open or half-shaded symbols) from hydrothermally treated grains of (**a**) sample CZ25 and (**b**) sample HZ5. In Figure 8b the data from dry isothermal annealing experiments with the same sample are shown for comparison (Geisler et al. 2001a; Geisler 2002).

linewidth and frequency of the $\nu_3(SiO_4)$ band does not terminate abruptly at the reaction front, but changes gradually across the boundary toward the interior of the grains (Figs. 2a and 9). The overall shape of the frequency- and linewidth-vs.-distance relationship resembles those of diffusion profiles (Figs. 9a, 9b). The Raman intensity of the $\nu_3(SiO_4)$ and the adjacent $\nu_1(SiO_4)$ band, however, decreases abruptly and significantly at the boundary (Fig. 9c). This observation is evidence that the diffusion-like profiles are not an artifact of a convolution of different contributions from recrystallized and unreacted areas due to volume resolution limitations. A given frequency of a molecular vibration in a crystalline solid probed by Raman spectroscopy can be affected by changes in (1) the average short-range order, (2) average compressive or tensile stress, or (3) by crystallite size (e.g., Fauchet 1986; Kitajima 1997). In the present case, a stress-induced frequency shift could be associated with the strong volume reduction resulting from the recrystallization of the amorphous phase inside the reaction rims. However, any stress imposed on a metamict zircon containing crystalline and amorphous material should lead to preferential strain in the amorphous rather than in the crystalline regions, because the amorphous material shows a significant higher compressibility compared to crystalline zircon (Chakoumakos et al. 1991; Lee and Tromp 1995). Furthermore, considering the experimentally determined pressure shift for the $\nu_3(SiO_4)$ mode of $d\omega/dP = 4.8 \pm 0.2$ cm^{-1}/GPa (Knittle and Williams 1993, compressive strain in the order of one GPa (i.e., still well below the tensile failure strength of about 2.1 GPa; Lee and Tromp 1995), for example, should also cause a significant frequency blue shift (i.e., ~4.8 cm^{-1}) of the $\nu_3(SiO_4)$ vibrations inside the rims that relaxes smoothly toward the surface (see also Izraeli et al. 1999). However, the frequency profiles from the reaction rim are flat or show a decreasing frequency toward the rim-core boundary. It is also evident from Figure 2b that we observed a sharp frequency decay toward the grain center in grains treated at 350 °C, although the reaction rims are heavily recrystallized. We thus propose that the smooth frequency shift across the boundary mainly reflects gradual differences in the average short-range order (i.e., in the defect density inside the crystalline material), possibly along with crystallite size effects (see Geisler et al. 2001a; Geisler and Pidgeon 2002). Based on this interpretation, it follows that the decoupled evolution of the frequency and the intensity of the $\nu_3(SiO_4)$ band seen in Figure 9 means that the sharp drop (within ~4 μm) of the intensity at the boundary largely reflects significant differences in the scattering volume between rim and core, i.e., differences in the fraction of crystalline material. If any contribution of the defect density inside the crystalline material to the Raman intensity is large compared to any differences in the fraction of crystalline material, we would also expect a gradual decay of the intensity across the boundary. We are aware that the Raman intensity is difficult to measure accurately, but note that the relative intensity is a reliable measure of the relative difference in the inherent scattering efficiency of the material as long as measurements are made under a given sample orientation and under the same analytical conditions. It is thus concluded that in the interior of the grains treated at high fluid temperatures (>550 °C), the disordered crystalline remnants have been partially annealed with no or only limited solid-state recrystallization. Such a conclusion is in line with the observation that most of the data from the low-CL cores plot along the first "dry" annealing stage in the frequency vs. linewidth diagram for the $\nu_3(SiO_4)$ band, which has been obtained from the same sample (Fig. 8).

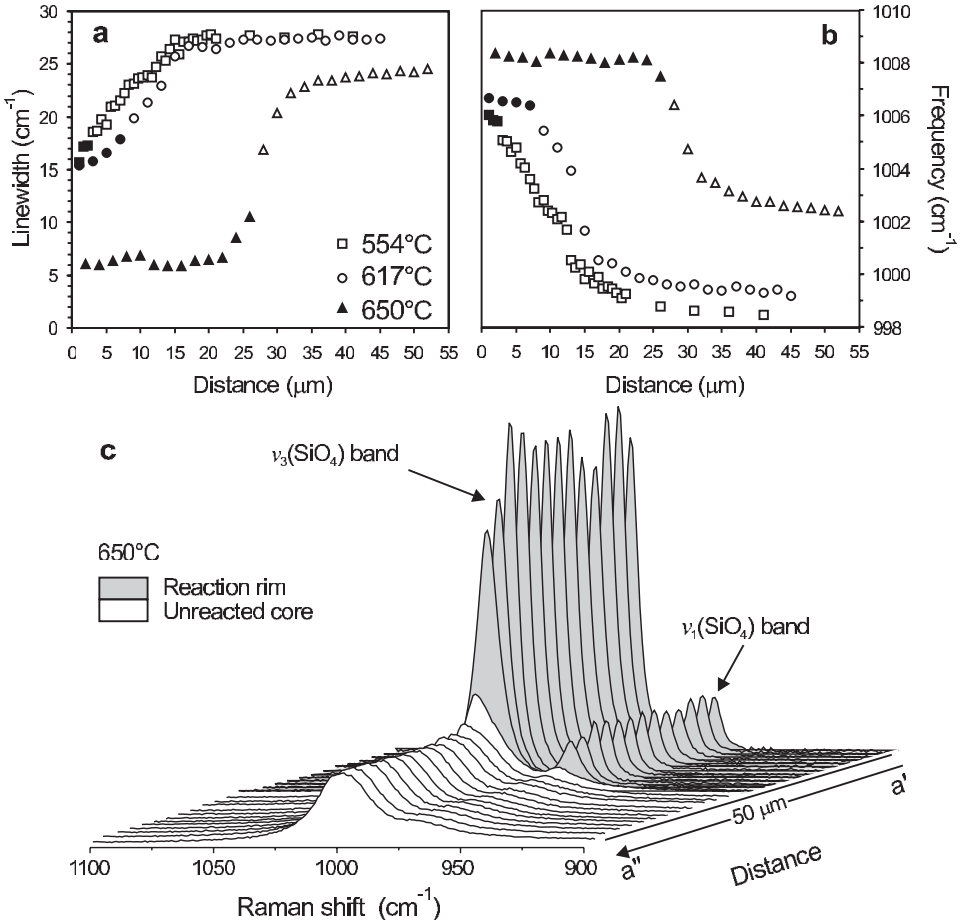

FIGURE 9. Raman line scans from grains of sample HZ5 (experiments no. 1g, no. 2g, and no. 3g) showing the change of (**a**) the width (given as full width at half maximum) and (**b**) the frequency of the asymmetrical $\nu_3(SiO_4)$ stretching band as a function of the distance from the grain surfaces. Black symbols represent data from the reaction zones whereas open symbols mark data which are located within the low-CL core areas. (**c**) Series of Raman spectra from a grain of sample HZ5 between 900 and 1100 cm^{-1} as a function of the distance from the grain surface. Spectra correspond to the 650 °C data (experiment no. 2g) shown in Figure 9a and b. A linear background was subtracted from the spectra. Note the sharp drop of the Raman intensity at the boundary between reaction rim and the low-CL core.

DISCUSSION

Hydrothermal alteration of partially metamict zircon

Dissolution-reprecipitation vs. solid state recrystallization and the role of water. The most striking result of the experimental study is the development of reaction zones on experimental zircon grains characterized by a systematic pattern of structural recovery. In particular, the extensive recrystallization of metamict zircon under hydrothermal conditions (Fig. 8) contrasts markedly with the degree of structural recovery seen in dry annealing studies at equivalent temperatures and time scales (Zhang et al. 2000a, 2000b; Geisler et al. 2001a, Geisler 2002). In principle, the reaction rims could be produced by a process of coupled dissolution-reprecipitation, as advocated by Putnis (2002) for various mineral replacement reactions. Such replacement reactions are believed to be controlled by the motion of a dissolution front — possibly characterized by a thin film of fluid — that separates the parent from the precipitated product phase and the exchange of components through the product phase. However, (1) the diffuse concentration profiles seen in some reaction zones (Figs. 2), (2) the formation of curved or ring patterns, indicative for a non-equilibrium situation typical for diffusion-reaction processes (e.g., Cross and Hohenberg 1993), (3) the occurrence of temperature-dependent, intermediate states of structural disorder (Fig. 8), and (4) the limited loss of radiogenic Pb seen in some high-temperature experiments with zircon HZ5 (see discussion below) can hardly be explained by such coupled process of dissolution and precipitation. Instead, the observed alteration features are more compatible with a model based on the diffusion of solute and solvent atoms from and into the metamict zircon. The enhanced rate of structural recovery processes, including recrystallization, under hydrothermal conditions compared with dry annealing demands for the presence of a catalyst, which readily entered the metamict zircon structure. We suggest that the enhanced kinetics of structural recovery processes

under hydrothermal conditions, including the experiment with pure water, was most likely the direct result of the diffusion of a water species into the metamict network. Penetration of water is believed to be the main driving force for the growth kinetics of the reaction-recrystallization fronts. However, it is not yet possible to give an atomistic description of the reaction. Support for this phenomenological interpretation is given by studies on the recrystallization behavior of amorphous titanates in a water vapor environment, which have shown that hydrogen, resulting from the dissociation of water at the surface of the titanate specimens, significantly reduces the activation energy to recrystallization (Simpson and Mitchell 1993; Simpson et al. 1994; Meldrum et al. 2002). Furthermore, the diffusion-like profiles of the frequency of the $\nu_3(SiO_4)$ stretching vibration across the reaction rims into the low-CL cores are evidence that the kinetics of the recovery process was not controlled solely by the fluid temperature. However, the idea of water diffusion apparently conflicts with the observed sharp boundary between core and reaction rim seen in the CL images. A way out of this dilemma may be that the amorphous material did not start to recrystallize until a temperature-dependent threshold concentration of water was reached. One may speculate that the water diffusion front moves ahead of the recrystallization front by some distance, and that only minute amounts of water were necessary to accelerate structural recovery processes. The profound effect of tiny amounts of water on structural relaxation processes is known from annealing studies with silicate glasses in water vapor (e.g., Davis and Tomozava 1995). Such a model could explain the sharpness of the fronts seen in the CL images (Fig. 1) as well as the diffusion-like Raman frequency profiles (Fig. 9), as the integrated SEM-CL emission from metamict and annealed zircon is largely controlled by the fraction of crystalline material (Geisler and Pidgeon 2001; Poller et al. 2002), which, according to the Raman data, is significantly larger in the reacted, i.e., recrystallized areas than in the low-CL cores.

Relationship between chemical alteration, solution composition and recrystallization. From Figures 2 and 6, it is evident that the loss of REE, U, and Th from the reacted areas is inversely correlated with temperature. The interpretation of this interesting observation is apparently not straightforward, as we used a 2 *M* $AlCl_3$ and a 1 *M* HCl-$CaCl_2$ solution and a 2 *M* $CaCl_2$ solution, in the low- (≤350°) and high-temperature experiments (>350 °C), respectively. Also the experimental duration and the fluid pressure were different in these experiments. Furthermore, during the 350 °C-experiments with $AlCl_3$, the silica tubes dissolved and pyrophyllite precipitated from the solution, which implies that the activity of $Si(OH)_4$ in the solution reached a steady state during the experiment that was controlled by the solubility product of pyrophyllite. The relative enrichment of SiO_2 seen in the outer rim in grains from the 350 °C-experiments (Fig. 2b) may thus be governed by the higher $Si(OH)_4$ activity in these experiments. Such an interpretation is in line with the observations that the leaching behavior of silicate glasses (e.g., Grambow and Müller 2001), as well as the solubility of zircon in hydrothermal fluids at high temperatures, is controlled by the $Si(OH)_4$ activity (Ayers and Watson 1991). It is also likely that the stability of zircon in the 175 °C experiment (Fig. 2c) was controlled by the solution chemistry. In general, the complex ZrO_2 vs. SiO_2 relationships seen in Figure 4a suggest that the fluid composition can have a strong impact on the chemical alteration characteristics. Thus, it may be tempting to attribute the behavior of the REE, U, and Th also to the differences in the fluid chemistry (i.e., pH, Eh, ionic strength, and available cations). However, some observations indicate that their behavior had to be rather independent of the solution chemistry. First of all, in most experiments the average loss of Th appears to be little higher than the loss of U (Fig. 6), although Th solubility in hydrothermal solutions is usually several orders of magnitude lower than the U solubility (Keppler and Wyllie 1990; Bailey and Ragnarsdottir 1994). Secondly, Wood (1990) suggested on the basic of thermodynamic calculations that the solubility of Y- and REE-chloride complexes increases with increasing fluid temperature. This result is in agreement with the experimental observations of Flynn and Burnham (1978), who have found that increasing chloride concentration results in an increase in the partitioning of the REE into an aqueous fluid phase relative to silicate melts at magmatic temperatures. We further note that the inward diffusion of Ca and Al follows a similar temperature behavior, i.e., at low temperatures the cations were able to diffuse to the reaction front (Fig. 2c), whereas at higher temperatures the Ca and Al concentration profiles decay more smoothly toward the front (Figs. 2a and 3a). Also, the limited loss of radiogenic Pb from sample HZ5 seen in the high-temperature experiments clearly indicates that a different fluid chemistry alone cannot account for the observed temperature dependence of the chemical alteration. We propose here that the elemental loss or gain observed at high fluid temperatures (Fig. 2a) is also controlled by the competition between the kinetics of macroscopic diffusion through the reaction rim and solid-state recrystallization. The complex reaction rims, consisting of a gray-CL zone progressing to a bright-CL zone, which were observed on grains of sample CZ5 subjected to hydrothermal conditions at 350 °C in an $AlCl_3$ solution (Fig. 1i), are highly significant in illustrating such competitive behavior (Fig. 2b). The outer dark-CL zone is characterized by extensive chemical changes, which can be attributed to long-range diffusion of chemical species while the initial degree of recrystallization remained low. We note that the trace-element profiles in the outer rim are very similar to those observed in the 175 °C experiments (Fig. 2c). In these experiments, the degree of recrystallization was low, as indicated by the Raman data (see also Fig. 8a). It was suggested that only the disordered crystalline remnants were partially recovered (Geisler et al. 2002). Because damage accumulation in both samples already passed the first percolation point (Salje et al. 1999), where volume swelling sets off dramatically (Trachenko et al. 2003), bulk diffusion may be enhanced due to the percolation of amorphous material. However, at 350 °C the degree of recrystallization eventually reached a high degree of recrystallization (i.e., passing the first percolation point in the opposite direction), resulting in a rapid slowing and then cessation of diffusion of elements at the inner boundary of the gray-CL zone. The extent of the recrystallization front at this point is likely approximated by the dip in the frequency and linewidth curves (Fig. 2b). The development of

the bright-CL zone indicates a continued penetration of water into the zircon accompanied by a continuation of structural recovery. This recovery included further overall water-catalyzed recrystallization within the gray-CL zone to produce the observed annealing curves with distinct segments for the bright and the gray zone (see Raman profiles of Fig. 2b). Under this model, the development of the gray-CL zone, with extensive chemical transport, was curtailed by the progression of recrystallization, whereas the continuation of water diffusion produced the bright-CL zone with similar smooth elemental profiles, as seen in the 650 °C experiment with sample HZ5 (Fig. 2a). The fact that only a single zone was developed around grains from sample HZ5 suggests that the dynamics of diffusion and recrystallization at 350 °C was different when compared with sample CZ25. The limited elemental loss or gain observed at high fluid temperatures (Fig. 2a), as well as inside the bright-CL rim of grains from sample CZ25 (Fig. 2b), can be explained by faster recrystallization kinetics compared to the kinetics of bulk diffusion. We propose that most of the REE, U, and Th atoms—as well as Zr and Si—were incorporated in the newly grown zircon phase before they could diffuse out of the zircon over macroscopic length scales, resulting in the observed flat element profiles. Accordingly, the affinity of the REE, U, and Th to substitute for Zr in the zircon lattice should also affect their behavior during hydrothermal alteration of metamict zircon. Such a picture is fully consistent with the preservation of the chemical characteristics of primary growth zones at high fluid temperatures as seen in some grains of sample CZ25.

Incorporation of water in the reaction zones. In discussing the incorporation of a water species in the reaction zones, it is relevant to first consider why the reaction zones of all experimental grains are clearly marked by sharp changes of both the BSE and CL intensity. Whereas changes in the CL emission in the reaction zones can be explained by a higher degree of crystallinity, as indicated by the Raman intensity (Geisler and Pidgeon 2001; Poller et al. 2002; Fig. 9), the experimentally generated lower BSE signal needs a different explanation because it mainly depends on the chemical composition of the material, i.e., on the mean atomic number. The effect is common to all experiments, suggesting that the BSE contrast is mainly due to the addition of water species to the reaction zones, providing a significant reduction in the mean atomic number, which is necessary to be detected by the BSE technique. Note that the chemical changes seen in Figure 2a near the surface of the grain within the reaction rim are not reflected in the BSE image of the same grain shown in Figure 1p. Support for this interpretation is provided by the commonly lower analytical totals of the EMP measurements of the reaction zones (Table 1).

It is unlikely that high amounts of molecular water or hydroxyl are structurally bound in the newly formed crystalline material because: (1) Caruba et al. (1985) have found that F is required to stabilize OH in the zircon structure, which was not available in the experimental fluid; (2) first-principle quantum-mechanical calculations have shown that the non-dissociative adsorption of water on the (100) face of crystalline zircon is strongly preferred with respect to the dissociative adsorption (Balan et al. 2001); and (3) the water content in natural crystalline zircon is usually low (Woodhead et al. 1991; Nasdala et al. 2001). Considering the cracked or porous structure seen in Figure 1p, a possible explanation for the low analytical totals is that some molecular water was retained within pores or microcracks. However, though conceivable, it appears to be more likely that most of the water, as OH (formed by hydrolysis of the amorphous silica network) and possibly as H_2O, was trapped and dissolved within interstitial amorphous remnants, which were found to still occur in partially annealed metamict zircon (e.g., Capitani et al. 2000). However, the exact water speciation as well as the its location, which relates to the question as to whether water is a true catalyst in a precise definition of the term, remains speculative and is a challenge for ongoing research.

Incorporation of non-formula elements in the reaction zones. The clear relationship between the size of the solvent cations such as Al^{3+}, Ca^{2+}, Ba^{2+}, Mg^{2+}, K^{+}, and Na^{+} and their concentration inside the reaction zones formed at high fluid temperature suggests, at first glance, that these cations were incorporated into the newly grown crystalline zircon because the observed ionic size dependence would be in agreement with relative solution energies derived from computer simulations (Akhtar and Waseem 2001). The different trends in the frequency vs. linewidth relationship of the $\nu_3(SiO_4)$ stretching band seen for Al- and Ca-rich reaction zones around sample CZ25 may indicate an influence of Al on the tetrahedral vibration, and thus that some Al was incorporated in the crystalline zircon. However, considering the Goldschmidt rule according to which substitution is only possible if the size of the ions does not differ by more than 15%, which is reflected by three times higher solution energies for the substitution of Zr^{4+} by Ca^{2+}, Ba^{2+}, and Mg^{2+} compared with the $Zr^{4+} \leftrightarrow REE^{3+}$ substitution (Akhtar and Waseem 2001), it is more likely that the divalent cations were dissolved within the amorphous matrix, where they may have locally stabilized the amorphous state (as may also be assumed for dissolved water). The ion exchange, including a water species inside the amorphous material, may thus qualitatively be compared with reactions observed in leaching experiments with silicate glasses (e.g., Petit et al. 1990; Bunker 1994; Grambow and Müller 2001). However, further research is necessary to gain an atomistic understanding of the ion-exchange reactions.

The behavior of radiogenic Pb. The extreme incompatibility of Pb^{2+} in the zircon structure is well known. Watson et al. (1997) commented that "the degree to which Pb^{2+} is excluded from zircon during growth from a dry, P_2O_5-free melt is surprising." However, Pb is the final product of a series of α-recoil events from parent U and Th, and is located within the amorphous regions or in an interstitial position elsewhere in the disordered crystalline structure. The valence state of the radiogenic Pb atoms is not known, but it is considered highly likely that such atoms are in the divalent state rather than the more oxidized, though more structurally compatible, tetravalent state (Watson et al. 1997). Unlike other constituent trace elements such as the REE, parental U and Th, and initial (common) Pb, radiogenic Pb has no systematic charge compensation and no equilibrium position in the lattice. It is not surprising, therefore, that the behavior of Pb in the zircon differs from the other trace elements. Our experimental results show that the radiogenic Pb is strongly removed from the recrystallized re-

action zones, mostly because of the incompatibility of Pb^{2+} in the newly grown zircon phase. In the case of the sample CZ25, Pb loss during the low- and high-temperature experiments was consistently high, up to almost complete loss in a number of analyses, which contrasts with a limited Pb loss from grains of HZ5 at the highest fluid temperatures (Fig. 5, Table 3). This finding indicates the significance of the initial degree of radiation damage and the temperature on the Pb loss behavior of zircon under hydrothermal conditions. Our results thus support the conclusion of Mezger and Krogstad (1997) based on observations of natural zircon systems that "high temperatures as they are known from parts of the Earth's crust do not cause as much Pb-loss as low temperatures where metamictization destroys the lattice and thus enhances the movement of Pb." The results also demonstrate experimentally a further comment by these authors that: "Once metamict zircons are reheated and recrystallized, Pb is largely rejected from the new crystal. However, parts of the crystal that were not strongly metamict keep most of their lead." A comparison of the behavior of grains of HZ5 and CZ25 in the high-temperature experiments is not simple, however, because some grains of HZ5 appear to have lost a high proportion of their U, whereas this is not as evident in grains of CZ25. The reason for the low degree of Pb loss from grains of sample HZ5 treated at fluid temperatures in excess of 600 °C is not yet clear, but may be a consequence of its initially slightly higher amount of residual crystalline domains compared with sample CZ25. One may speculate that the initial effective diffusion of radiogenic Pb was most likely slower in sample HZ5, and that it also took less time for the growing crystalline domains to collide with each other, allowing Pb atoms to be trapped inside amorphous pockets.

Origin of internal patterns and fluctuations of the reaction front morphology. There is little doubt that the sharp parallel bands seen in the CL images of hydrothermally treated grains of sample CZ25 (e.g., Figs. 1f and 1g) reflect the primary growth-zoning pattern, which indicates that parts of the large grain of this sample are strongly heterogeneous. As there was almost no CL emission from the starting material, we could not detect this type of primary zoning by CL imaging prior to the experiments. However, we observed such growth banding by CL imaging after having heated some grains of this sample to temperatures as high as 1350 °C in a furnace under atmospheric conditions (unpublished data). Note that the preservation of primary growth zones in the hydrothermally treated grains can hardly be explained by a coupled dissolution-reprecipitation process. Because Raman spectroscopic measurements reveal that the degree of structural recovery in these zones is very similar, the CL contrast in these primary growth zones may be the result of primary differences in the REE (i.e., Dy^{3+} and Tb^{3+}) concentration. On the other hand, the localized faint ring patterns seen in the center of some grains of sample CZ25 (arrows in Figs. 1f and 1g) clearly point to a disequilibrium situation in the reacted zircon, again pointing to a diffusion-driven reaction process (e.g., Cross and Hohenberg 1993). Such patterns may reflect local chemical or structural fluctuations. However, based on the sharp contrast between the individual primary growth zones, which indicates limited diffusion-driven fading of the primary REE concentrations, it appears to be more likely that the diffuse ring patterns reflect small local fluctuations in the degree of recrystallization rather then variations in the REE concentrations. We further note that the fingering and scalloped front morphologies seen in some experiments are also in agreement with the notion of spatial self-organization (e.g., Ortoleva et al. 1987). In some cases, such structures can easily be explained by the formation of fractures (e.g., Fig. 1i–1l), as also discussed in Geisler et al. (2002). However, for other cases such as those seen in sample HZ5 (Fig. 1m–1o), the origin of the instabilities that caused the scalloped front morphology is not evident. Further research is necessary to understand these interesting types of spatial self-organization in hydrothermally treated metamict zircon.

The experimental reaction structures and analogies with natural systems

The core-rim structures, recrystallization patches and lobes (Figs. 1j–1l) as well as the fine ring structures (Figs. 1f and 1g) developed during the experimental hydrothermal treatment of the two zircon samples are similar to recrystallization structures observed in zircon grains from a number of different geological settings. For example, patchy recrystallization structures resemble altered patches in zircon grains from Archean granites (e.g., Pidgeon 1992), and the simple core-reaction rim structures resemble bright-luminescent, low-U overgrowths on zircon from a biotite gneiss from the Lewisian of Scotland (Kinny and Friend 1997). The ring structures seen in some experimental grains (Figs. 1e and 1f) are similar to those observed in zircon grains from granites of the Darling Range batholith by Pidgeon et al. (1998, Figs. 2h and 2j therein). Also, CL images of natural recrystallization zones or rims commonly reveal a number of internal reaction-recrystallization fronts (e.g., Vavra et al. 1996, 1999; Schaltegger et al. 1999). The bright-CL inner zone seen in the 350 °C experiments (Fig. 1l) resemble bright-CL recrystallization zones described by Hoskin and Black (2000) in zircon crystals from high-grade metagranites from Queensland, Australia, which they interpreted as recrystallization fronts produced under dry and isochemical conditions. Note also that milky-white zircon grains such as those seen in Figure 1a were already described by Grünenfelder (1963) and recently by Högdahl et al. (2001).

Although, as shown above, the internal structures from many natural zircon crystals show similarities with those produced in the hydrothermal experiments, the age of the secondary structures often post-dates the primary crystallization from a magma (e.g., Pidgeon 1992; Nemchin and Pidgeon 1997) or the peak of metamorphism by only a few million years (e.g., Schaltegger et al. 1999; Vavra et al. 1996, 1999; Tomaschek et al. 2001), so that the zircon grains were not metamict at the time of the recrystallization event. Although this may be explained in some cases by the fact that the reaction rims seen in natural zircon were produced over an extended period of geological time, so that even little-damaged crystals may react with a fluid (Geisler et al. 2001b), the similarity between experimentally produced and natural structures does not mean that radiation damage is the only necessary prerequisite. An important factor in decreasing the stability of zircon could be significant lattice strain associated with the incorporation of high concentrations of trace

elements such as a xenotime component, which forms a limited solid solution with $ZrSiO_4$. In such zircon, the driving force for the zircon-fluid reaction could be the reduction of the free energy associated with the removal of these trace elements (e.g., Tomaschek et al. 2001).

A crucial problem in modern SIMS zircon geochronology is linked to the question of when recrystallization zones are formed during a metamorphic cycle—a question that is important when using zircon for the reconstruction of *P-T-t* paths in metamorphic basement rocks. Because we believe that water is necessary as a "catalyst" for the formation of recrystallization fronts, this question is in turn connected to the availability of water. We would like to emphasize that it is also likely that the recrystallization rims or fronts observed in natural zircon can be produced not only by the interaction with a free hydrothermal fluid, which is certainly available during prograde metamorphic conditions when dehydration reactions occur, but also by diffusion of water from an interstitial fluid film, from surrounding hydrous minerals, or from a hydrous partial melt.

ACKNOWLEDGMENTS

Many thanks go to P. Chapman for his support with the Raman spectrometer, to B. Cornelisen for her assistance during the electron microprobe work, B. Mihailova for her help with the IR spectrometer, and to A. Kennedy and A. A. Nemchin for their support during the SHRIMP sessions. We acknowledge J. Schlüter from the Mineralogical Museum of the University of Hamburg for providing the sample HZ5 used in this study, and A. Mutter, K. Pollok, A. Putnis, S. Ríos, E.K.H. Salje, F. Tomaschek, and M. Zhang for stimulating discussions, which help to clarify conclusion drawn in the paper. We also appreciate the constructive reviews of two anonymous journal reviewers, which helped to improve the final manuscript. TG acknowledges financially support from the Deutsche Forschungsgemeinschaft (DFG), project GE 1094/1-1 and GE 1094/1-2.

REFERENCES CITED

Akhtar, M.J. and Waseem, S. (2001) Atomistic simulation studies of zircon. Chemical Physics, 274, 109–120.

Ayers, J.C. and Watson, E.B. (1991) Solubility of apatite, monazite, zircon and rutile in supercritical aqueous fluids with implications for subduction zone geochemistry. Philosophical Transactions Royal Society of London, A335, 365–375.

Bailey, E.H. and Ragnarsdottir, K.V. (1994) Uranium and thorium solubilities in subduction zone fluids. Earth Planetary Science Letters, 124, 119–129.

Balan, E., Mauri, F., Muller, J.-P., and Calas, G. (2001) First principles study of water adsorption on the (100) surface of zircon : Implications for zircon dissolution. American Mineralogist, 86, 910–914.

Bunker, B.C. (1994) Molecular mechanisms for corrosion of silica and silicate glasses. Journal of Non-Crystalline Solids, 179, 300–308.

Capitani, G.C., Leroux, H., Doukhan, J.C., Ríos, S., Zhang, M., and Salje, E.K.H. (2000) A TEM investigation of natural metamict zircons: structure and recovery of amorphous domains. Physics and Chemistry of Minerals, 27, 545–556.

Caruba, R., Baumer, A., Ganteaume, M., and Iacconi, P. (1985) An experimental study of hydroxyl groups and water in synthetic and natural zircons: a model of the metamict state. American Mineralogist, 70, 1224–1231.

Chakoumakos, B.C., Oliver, W.C., Lumpkin, R.C., and Ewing, R.C. (1991) Hardness and elastic modulus of zircon as a function of heavy-particle irradiation dose: I. *In situ* α-decay event damage. Radiation Effects and Defects in Solids, 118, 393–403.

Cherniak, D.J., Hanchar, J.M., and Watson, E.B. (1997) Diffusion of tetravalent cations in zircon. Contributions to Mineralogy and Petrology, 127, 383–390.

Claoué-Long, J.C., Compston, W., Roberts, J., and Fanning, C.M. (1995) Two Carboniferous ages: a comparison of SHRIMP zircon dating with conventional zircon ages and $^{40}Ar/^{39}Ar$ anayses: geochronology, time scales and global stratigraphic correlation. Society of Sedimentary Geology, Special Publications, 54, 3–21.

Colombo, M., Chrosch, J., and Salje, E.K.H. (1999) Annealing metamict zircon: a powder X-ray diffraction study of a highly defective phase. Journal of the American Ceramic Society, 82, 2711–2716.

Compston, W., Williams, I.S., and Meyer, C. (1984) U-Pb geochronolgy of zircons from the lunar breccia 73217 using a sensitive high-resolution ion microprobe. Proceedings XIV Lunar Planetary Science Conference. Journal of Geophysical Research, 89, B525–B534.

Cross, M.C. and Hohenberg, P.C. (1993) Pattern formation outside equilibrium. Reviews in Modern Physics, 65, 851–1112.

Davis, K.M. and Tomozawa, M. (1995) Water diffusion into silica glass: structural changes in silica glass and their effect on water solubility and diffusivity. Journal of Non-Crystalline Solids, 185, 203–220.

DeLaeter, J.R. and Kennedy, A.K. (1998) A double focusing mass spectrometer for geochronology. International Journal of Mass Spectrometry and Ion Processes, 178, 43–50.

Ewing, R.C., Lutze, W., and Weber, W.J. (1995) Zircon: A host phase for the disposal of weapons plutonium. Journal of Materials Research, 10, 243–246.

Farnan, I. and Salje, E.K.H. (2001) The degree and nature of radiation damage in zircon observed by ^{29}Si nuclear magnetic resonance. Journal of Applied Physics, 89, 2084–2090.

Fauchet, P.M. (1986) Mapping solid surfaces with a Raman microprobe. Scanning Electron Microscopy, II, 425–435.

Flynn, R.T. and Burnham, C.W. (1978) An experimental determination of rare earth partition coefficients between a chloride containing vapor phase and silicate melts. Geochimica Cosmochimica Acta, 42, 685–701.

Geisler, T. (2002) Isothermal annealing of partially metamict zircon: evidence for a three-stage process. Physics and Chemistry of Minerals, 29, 420–429.

Geisler, T. and Schleicher, H. (2000) Improved U-Th-total Pb dating of zircons by electron microprobe using a new background modeling method and Ca as a chemical indicator of fluid-induced U-Th-Pb discordance in zircon. Chemical Geology, 163, 269–285.

Geisler, T. and Pidgeon, R.T. (2001) Significance of radiation damage on the integral SEM cathodoluminescence intensity of zircon: an experimental study. Neues Jahrbuch für Mineralogie, Monatshefte, 10, 433–445.

Geisler, T. and Pidgeon, R.T. (2002) Raman scattering from metamict zircon: Comments on "Metamictisation of natural zircon: accumulation versus thermal annealing of radioactivity-induced damage" by Nasdala et al., 2001 (Contributions to Mineralogy and Petrology, 141, 125–144). Contributions to Mineralogy and Petrology, 143, 750–755.

Geisler, T., Pidgeon R.T., van Bronswijk, W., and Pleysier, R. (2001a) Kinetics of thermal recovery and recrystallization of partially metamict zircon: a Raman spectroscopic study. European Journal of Mineralogy, 13, 1163–1176.

Geisler, T., Ulonska, M., Schleicher, H., Pidgeon, R.T., and van Bronswijk, W. (2001b) Leaching and differential recrystallization of metamict zircon under experimental hydrothermal conditions. Contributions to Mineralogy and Petrology, 141, 53–65.

Geisler, T., Pidgeon, R.T., van Bronswijk, W., and Kurtz, R. (2002) Transport of uranium, thorium, and lead in metamict zircon under low-temperature hydrothermal conditions. Chemical Geology, 191, 141–154.

Geisler, T., Rashwan, A.A., Rahn, M.K.W., Poller, U., Zwingmann, H., Pidgeon, R.T., Schleicher, H., and Tomaschek F. (2003) Low-temperature hydrothermal alteration of natural metamict zircons from the Eastern Desert, Egypt. Mineralogical Magazine, 67, 485–507.

Grambow, B. and Müller, R. (2001) First order dissolution rate and the role of glass surface layers in glass performance assessment. Journal of Nuclear Materials, 298, 112–124.

Grünenfelder, M. (1963) Heterogenität akzessorischer Zirkone und die petrogenetische Deutung ihrer Uran/Blei-Zerfallsalter. I. Der Zirkon des Granodioritgneises von Acquacalda (Lukmanierpass). Schweizer Mineralogisch-Petrographische Mitteilungen, 43, 235–257.

Högdahl, K., Gromet, L.P., and Broman, C. (2001) Low *P-T* Caledonian resetting of U-rich Paleoproterozoic zircons, central Sweden. American Mineralogist, 86, 534–546.

Hoskin, P.W.O. and Black, L.P. (2000) Metamorphic zircon formation by solid-state recrystallization of protolith igneous zircon. Journal of Metamorphic Geology, 18, 423–439.

Izraeli, E.S., Harris, J.W. and Navon, O. (1999) Raman barometry of diamond formation. Earth and Planetary Science Letters, 173, 351–360.

Keppler, H. and Wyllie, P.J. (1990) Role of fluids in transport and fractionation of uranium and thorium in magmatic processes. Nature, 348, 531–533.

Kinny, P.D. and Friend, C.R.L. (1997) U-Pb isotopic evidence for the accretion of different crustal blocks to form the Lewisian Complex of north-west Scotland. Contributions to Mineralogy and Petrology, 129, 326–340.

Kitajima, M. (1997) Defects in crystals studied by Raman scattering. Critical Reviews in Solid State and Material Sciences, 22, 275–349.

Knittle, E. and Williams, Q. (1993) High-pressure Raman spectroscopy of $ZrSiO_4$: Observation of the zircon to scheelite transition. American Mineralogist, 78, 245–252

Lee, L.K.W. and Tromp, J. (1995) Self-induced fracture generation in zircon. Journal of Geophysical Research, 100, B9, 17753–17770.

Mathieu, R., Zetterstrom, L., Cuney, M., Gauthier-Lafaye, F. and Hidaka, H. (2001) Alteration of monazite and zircon and lead migration as geochemical tracers of fluid paleocirculations around the Oklo–Okélobondo and Bangombe natural nuclear reaction zones (Franceville basin, Gabon). Chemical Geology, 171, 147–171.

Medenbach, O. (1976) Geochemie der Elemente in Zirkon und ihre räumliche Verteilung – Eine Untersuchung mit der Elektronenstrahlmikrosonde. Ph.D. thesis, Ruprecht-Karl-Universität, Heidelberg, Germany.

Meldrum, A., Boatner, L.A., Weber, W.J., and Ewing, R.C. (2002) Amorphization and recrystallization of the ABO_3 oxides. Journal of Nuclear Materials, 300, 242–254.

Mezger, K. and Krogstad, E.J. (1997) Interpretation of discordant U-Pb ages: An evaluation. Journal of Metamorphic Geology, 15, 127–140.

Murakami, T., Chakoumakos, B.C., Ewing, R.C., Lumkin, G.R., and Weber, R.W.J. (1991) Alpha-decay event damage in zircon. American Mineralogist, 76, 1510–1532.

Nasdala, L., Irmer, G., and Wolf, D. (1995) The degree of metamictization in zircon: a Raman spectroscopic study. European Journal of Mineralogy, 7, 471–478.

Nasdala, L., Beran, A., Libowitky, E., and Wolf, D. (2001) The incorporation of hydroxyl groups and molecular water in natural zircon ($ZrSiO_4$). American Journal of Science, 301, 831–857.

Nelson, D.R. (1997) Compilation of SHRIMP U-Pb zircon geochronology data, 1996. Geological Survey of Western Australia, Rec. 1997/2, 198 pp.

Nemchin, A.A. and Pidgeon, R.T. (1997) Evolution of the Darling Range Batholith, Yilgarn Craton, Western Australia: a SHRIMP zircon study. Journal of Petrology, 38, 625–649.

Ortoleva, P., Merino, E., Moore, G., and Chadam, J. (1987) Geochemical self-organization I: Reaction-transport feedbacks and modeling approach. American Journal of Science, 287, 979–1007.

Petit, J.-C., Della Mea G., Dran, J.-C., Magonthier, M.-C., Mando, P.A., and Paccagnella, A. (1990) Hydrated-layer formation during dissolution of complex silicate glasses and minerals. Geochimica and Cosmochimica Acta, 54, 1941–1955.

Pidgeon, R.T. (1992) Recrystallization of oscillatory zoned zircon: some geochronological and petrological implications. Contribution to Mineralogy and Petrology, 110, 463–472.

Pidgeon, R.T., O'Neil, J.R., and Silver, R.T. (1966) Uranium and lead isotopic stability in a metamict zircon under experimental hydrothermal conditions. Science, 154, 1538–1540.

——— (1973) Observations on the cristallinity and the U-Pb system of a metamict Ceylon zircon under experimental hydrothermal conditions. Fortschritte in der Mineralogie, 50, 118.

Pidgeon, R.T., Furfaro, D., Kennedy, A.K., Nemchin, A.A., and van Bronswijk, W. (1994) Calibration of zircon standards for the Curtin SHRIMP II. 8th International Conference on Geochronology, Cosmochronology and Isotope Geology. US Geological Survey Circular, 1107, 251.

Pidgeon, R.T., O'Neil, J.R., and Silver, R.T. (1995) The interdependence of U-Pb stability, crystallinity and external conditions in natural zircons – an early experimental study. In Leon T. Silver 70th Birthday Symposium and Celebration. Pasadena, CA: California Institute of Technology (Extended Abstract), 225–231.

Pidgeon, R.T., Nemchin, A.A., and Hitchen, G.J. (1998) Internal structures of zircons from Archean granites from the Darling Range batholith: implications for zircon stability and the interpretation of zircon U-Pb ages. Contributions to Mineralogy and Petrology, 132, 288–299.

Pidgeon, R.T., Macambira, M.J.B., and Lafon, J.-M. (2000) Th-U-Pb isotpic system and internal structures of complex zircons from an enderbite from the Pium Complex, Carajás Province, Brazil: evidence for the ages of granulite facies metamorphism and the protolith of the enderbite. Chemical Geology, 166, 159–171.

Poller, U., Geisler, T., Huth, J., and Pidgeon, R.T. (2002) Understanding CL in natural zircons. Goldschmidt Conference Abstracts, A609.

Putnis, A. (2002) Mineral replacement reactions: from macroscopic observations to microscopic mechanisms. Mineralogical Magazine, 66, 689–708.

Ríos, S., Salje, E.K.H., Zhang, M., and Ewing, R.C. (2000) Amorphization in zircon: evidence for direct impact damage. Journal of Physics C, 12, 2401–2412.

Rizvanova, N.G., Levchenkov, O.A., Belous, A.E., Bezmen, N.I., Maslenikov, A.N., Komarov, A.N., Makeev, A.F., and Levskii, L.K. (2000) Zircon reaction and stability of the U-Pb isotope system during interaction with carbonate fluid: experimental hydrothermal study. Contributions to Mineralogy and Petrology, 139, 101–114.

Salje, E.K.H., Chrosch, J., and Ewing, R.C. (1999) Is "metamictization" of zircon a phase transition? American Mineralogist, 84, 1107–1116.

Schaltegger, U., Fanning, C.M., Günther, D., Maurin, J.C., Schulmann, K., and Gebauer, D. (1999) Growth, annealing and recrystallization of zircon and preservation of monazite in high-grade metamorphism: conventional and in-situ U-Pb isotope, cathodoluminescence and microchemical evidence. Contributions to Mineralogy and Petrology, 134, 186–201.

Shannon, R.D. (1976) Revised effective ionic radii and systematic studies of interatomic distances in halides and chalcogenides. Acta Crystallographica, A32, 751–767.

Silver, L.T. and Deutsch, S. (1963) Uranium—lead isotopic variations in zircons—a case study. Journal of Geology, 71, 721–758.

Simpson, T.W. and Mitchell, I.V. (1993) Hydrogen assisted crystallisation of strontium titanate. Nuclear Instruments and Methods in Physics Research, B80/81, 1178–1181.

Simpson, T.W., Mitchell, I.V., McCallum, J.C., and Boatner, L.A. (1994) Hydrogen catalyzed crystallization of strontium titanate. Journal of Applied Physics, 76, 2711–2718.

Sinha, A.K., Wayne, D.M., and Hewitt, D.A. (1992) The hydrothermal stability of zircon: Preliminary experimental and isotopic studies. Geochimica et Cosmochimica Acta, 56, 3551–3560.

Stern, T.W., Goldich, S.S., and Newell, M.F. (1966) Effects of weathering on the U/Pb ages of zircons from the Morton Gneiss, Minnesota. Earth Planetary Science Letters, 1, 369–371.

Tomaschek, F., Kennedy, A., Villa, I., Lagos, M., and Ballhaus, C. (2001) Case study of metamorphisc zircons from Alpine HP/LT metamorphic rocks of Syros, Cyclades, Greece. EUG, Journal Conference Abstracts, 6, 768.

Townsend, P.D., Karali, T., Rowlands, A.P., Smith, V.A., and Vazquez, G. (1999) Recent examples of cathodoluminescence as a probe of surface structure and composition. Mineralogical Magazine, 63, 211–226.

Trachenko, K., Dove, M., and Salje, E.K.H. (2002) Structural changes in zircon under α-decay irradiation. Physical Review B, 65, 180102 (R).

——— (2003) Large swelling and percolation in irradiated zircon. Journal of Physics: Condensed Matter, 15, L1–L7.

Vavra, G., Gebauer, D., Schmid, R., and Compston, W. (1996) Multiple zircon growth and recrystallization during polyphase Late Carboniferous to Triassic metamorphism in granulites of the Ivrea Zone (Southern Alps): an ion microprobe (SHRIMP) study. Contributions to Mineralogy and Petrology, 122, 337–358.

Vavra, G., Schmid, R., and Gebauer, D. (1999) Internal morphology, habit and U-Th-Pb microanalysis of amphibolite-to-granulite facies zircons: geochronology of the Ivrea Zone (Southern Alps). Contributions to Mineralogy and Petrology, 134, 380–404.

Watson, B., Cherniak, D.J., Hanchar, J.M., Harrison, T.M., and Wark, D.A. (1997) The incorporation of Pb into zircon. Chemical Geology, 141, 19–31.

Weber, W.J., Ewing, R.C., and Wang, L.-M. (1994) The radiation-induced crystalline-to-amorphous transition in zircon. Journal of Materials Research, 9, 688–698.

Wood, S.A. (1990) The aqueous chemistry of rare-earth elements and yttrium, 2. Theoretical predictions of speciation in hydrothermal solutions to 350 °C at saturation water vapor pressure. Chemical Geology, 88, 99–125.

Woodhead, J.A., Rossman, G.R., and Silver, L.T. (1991) Hydrous species in zircon. American Mineralogist, 76, 1533–1546.

Zhang, M. and Salje, E.K.H. (2001) Infrared spectroscopic analysis of zircon: Radiation damage and the metamict state. Journal of Physics Condensed Matter, 13, 3057–3071.

Zhang, M., Salje, E.K.H., Capitani, G.C., Leroux, H., Clark, A.M., Schlüter, J., and Ewing R.C. (2000a) Annealing of α-decay damage in zircon: a Raman spectroscopic study. Journal of Physics Condensed Matter, 12, 3131–3148.

Zhang, M., Salje, E.K.H., Ewing, R.C., Farnan, I., Ríos, S., Schlüter, J., and Leggo, P. (2000b) Alpha-decay damage and recrystallization in zircon: evidence for an intermediate state from infrared spectroscopy. Journal of Physics Condensed Matter, 12, 5189–5199.

Zhang, M., Salje, E.K.H., Farnan, I., Graeme-Barber, A., Daniel, P., Ewing, R.C., Clark, A. M., Ríos, S., and Leroux, H. (2000c) Metamictization of zircon: Raman spectroscopic study. Journal of Physics Condensed Matter, 12, 1915–1925.

MANUSCRIPT RECEIVED SEPTEMBER 26, 2002
MANUSCRIPT ACCEPTED MAY 9, 2003
MANUSCRIPT HANDLED BY GREGORY LUMPKIN